Binary black hole mergers in gaseous disks: Simulations in general relativity

Brian D. Farris, Yuk Tung Liu, and Stuart L. Shapiro*

Department of Physics, University of Illinois at Urbana-Champaign, Urbana, Illinois 61801, USA

(Received 12 May 2011; published 14 July 2011)

Simultaneous gravitational and electromagnetic wave observations of merging black hole binaries (BHBHs) can provide unique opportunities to study gravitation physics, accretion, and cosmology. Here we perform fully general-relativistic, hydrodynamic simulations of equal-mass, nonspinning BHBHs coalescing in a circumbinary disk. We evolve the metric using the Baumgarte-Shapiro-Shibata-Nakamura (BSSN) formulation of Einstein's field equations with standard moving puncture gauge conditions. We handle the hydrodynamics via a high-resolution shock-capturing scheme. These initial simulations are exploratory in nature and simplified accordingly. We track the inspiral starting from a binary separation of $10M$, where M is the total binary mass. We take the disks to have an inner radius at $R_{\rm in} \approx 15M$ to account for the hollow created by the binary torques. Our disks extend to $R \approx 65M$ and have an initial scale height of $H/R \approx 0.03$–0.11. The gas is governed by a Γ-law equation of state, with Γ equal to $5/3$, $4/3$, and 1.1. Disks are allowed to relax in the ''early inspiral'' epoch to provide quasistationary realistic initial data. We then evolve the spacetime metric and matter during the ''late inspiral and merger'' epochs. The later simulations are designed to track BHBH inspiral following disk-binary decoupling, through merger and ringdown, terminating before viscosity has time to fill the hollow about the black hole remnant. We compute the gas flow and accretion rate and estimate the electromagnetic luminosity due to bremsstrahlung and synchrotron emission as a perturbation for optically thin disks. The synchrotron component of the luminosity peaks in the infrared band and should be detectable by WFIRST and possibly the LSST for a $10^8 M_\odot$ binary embedded in a disk with a density $n \sim 10^{12}$ cm^{-3} at $z = 1$, beginning with a maximum value of $L \sim 10^{46} n_{12}^2 M_8^3$ erg s^{-1} at decoupling, and decreasing steadily over a time scale of $\sim 100 M_8$ hours to a value of $L \sim 10^{45} n_{12}^2 M_8^3$ erg s^{-1} at merger.

DOI: 10.1103/PhysRevD.84.024024 PACS numbers: 04.25.D−, 04.25.dg, 47.75.+f

I. INTRODUCTION

All bulge galaxies (including the Milky Way) are believed to contain a central supermassive black hole with a mass M between $10^4 M_\odot$ and $10^9 M_\odot$ [1–3]. It is also believed that galaxy mergers commonly lead to the formation of a massive black hole binary (BHBH) system in the merged remnants [4,5]. In the standard picture, the BHBH binary separation decreases, first through dynamical friction due to distant stellar encounters, then through gravitational slingshot interactions in which nearby stars are ejected at velocities comparable to the binary's orbital velocity, and finally through the emission of gravitational radiation, leading to coalescence of the binary [6]. These low-frequency gravitational waves will be detectable by LISA (Laser Interferometer Space Antenna) and will contain a wealth of information about the inspiral. The gaseous accretion flow that forms around the binary can be a source of electromagnetic radiation as well. Following the detection of gravitational waves from a BHBH merger, electromagnetic ''afterglow'' radiation can provide confirmation of the coalescence [7–13]. The time scale during which detectable afterglow radiation rises to its maximum is governed by viscous diffusion of gas close to the remnant and ranges from several years to hundreds of decades in the case of supermassive BHBH systems.

There also exists the possibility of detecting electromagnetic ''precursor'' radiation prior to the merger and before the maximum gravitational wave emission [14,15]. If the merger takes place in a hot gas cloud in which the distant gas is nearly homogeneous and either at rest with respect to the binary (''binary Bondi'' accretion) or moving (''binary Bondi-Hoyle-Lyttleton'' accretion), then Farris *et al.* [16] (hereafter Paper I) have shown that the luminosity will peak at the end of the binary inspiral phase immediately prior to the final plunge. At this stage shock heating of the gas and turbulent magnetic field amplification are strongest. The peak luminosity lasts for $\delta t \sim M_6$ hours prior to merger and then plummets sharply following the coalescence. Here M_6 is the binary mass in units of $10^6 M_\odot$. If, instead, the accretion takes place via a geometrically thin, optically thick Keplerian disk around the binary (''binary Shakura-Sunyaev'' accretion), there may be a late-time precursor brightening from tidal and viscous (or turbulent magnetic) dissipation in the inner disk. This radiation peaks on a time scale of $\delta t \sim 0.1 M_6$ days prior to merger and remains high afterwards [15]. Each of these scenarios raises the exciting possibility of a simultaneous detection of electromagnetic and gravitational waves from a BHBH merger.

This picture is loosely supported by a number of observed active galactic nuclei (AGNs) that may be harboring

*Also at Department of Astronomy & NCSA, University of Illinois at Urbana-Champaign, Urbana, IL 61801.

 © 2011 American Physical Society

BHBH binaries. Very-long base line interferometry (VLBI) observations of the elliptical galaxy 0402+379 have discovered two radio sources at a projected separation of only 7 pc. The existence of jets, as well as variability associated with BH activity, indicate that the system may be a BHBH binary [17–19]. Another candidate is OJ 287, a BL Lac object whose light curve shows variability with a period of ~12 yr. It is believed that this may be a massive BHBH binary around which the smaller BH orbits with a period of 12 yr, penetrating the disk of the primary and giving rise to the observed variability [20–22]. It has been proposed that the quasar SDSS 092712.65+294344 may be either a binary system [23,24], or a recoiling BH which is the product of a binary merger [25]. Such suggestions are supported by a systematic shift of 2650 $\mathrm{km\,s^{-1}}$ in the emission lines. Another candidate is quasar SDSS J153636.22+044127.0, in which two broad line emission systems are observed, separated in velocity by 3500 $\mathrm{km\,s^{-1}}$. This observation has been interpreted as a BHBH binary system in which each object has its own emission system [26]. Recently, the first triple AGN system, SDSS J1027+1749, has been discovered [27]. This galaxy contains three emission line nuclei corresponding to a supermassive black hole triple with kpc-scale separations.

Information from a simultaneous detection of electromagnetic and gravitational waves may be useful for studying fundamental aspects of gravitational physics. For example, in some modified gravity scenarios, the propagation velocity for gravitons may differ from that of photons [28,29]. Additionally, the measurement of the luminosity distance from the gravitational wave signal at an accuracy of 1%–10%, coupled with the redshift information from the electromagnetic detection, could serve as a cosmological ''standard siren'' of unprecedented accuracy (better than ~1%) [30]. Such detections may also combine accurate measurements of BH spins and masses obtained from gravitational wave signals with electromagnetic observations to probe BH accretion physics in great detail [31]. It has even been proposed that simultaneous detections of electromagnetic and gravitational waves may provide a means of witnessing the birth of a quasar [32].

Several mechanisms for electromagnetic emission from accretion disks around merging BHBH binaries have been proposed. In one scenario, the inner edge of the accretion disk is identified as the radius at which the viscous torque on the gas balances the gravitational torque from binary. This radius is between 1.5 and 2 times the orbital separation [33–36] and encompasses a hollow region in the disk. Late in the inspiral the BHBH binary decouples from the disk and coalesces. For a binary of mass $M \approx 10^6 M_\odot$ accreting at 10% of the Eddington rate, the subsequent evolution of this disk, which is optically thick, gives rise to a source that initially peaks in the UV band and then hardens to extreme ultraviolet and soft x-ray emission at late times [7,12,13]. Additionally, there is a sudden change in the mass of the binary during the final stage of the merger, as gravitational waves carry away a few percent of the mass. The abrupt change in the potential creates waves in the disk which may grow into shocks and increase the luminosity of the disk in a unique way [10,11,37], giving rise to a detectable prompt x-ray signal. Another possibility is that the merged BH remnant may experience a recoil velocity which can, in principle, be as high as several thousand $\mathrm{km\ s^{-1}}$ [38], although it is likely to be much lower (<200 km/s) in most galaxy mergers [39]. This recoiling BH may ''shake'' or penetrate the disk, creating shocks which could give rise to a transient signal.

Various methods have been used to model plausible sources of electromagnetic emission from BH mergers. In one approach, the dynamics of the inspiral is ignored, focusing on the effect of BH kicks and/or BH mass loss on the hydrodynamical flow [8–11,37,40–43]. In another approach, the behavior of the gas is modeled by following the motion of collisionless ''particle tracers'' on geodesics [44]. Other approaches involve vacuum and/or force-free calculations to investigate the role that magnetic fields may play in producing detectable electromagnetic emission when the density near the binary at merger is very low [45,46]. Only recently have fully relativistic, hydrodynamical simulations of BHBH binary inspiral and merger in a gaseous environment been performed [16,47–49].

In this paper we study BHBH binary mergers in the presence of a circumbinary gaseous disk. Modeling such systems requires fully general-relativistic dynamical simulations. The development of stable algorithms to integrate Einstein's field equations of general relativity numerically in $3+1$ dimensions, such as the Baumgarte-Shapiro-Shibata-Nakamura (BSSN) formalism [50,51] and the generalized harmonic approach [52–54], together with the identification of suitable gauge conditions, has enabled several pioneering simulations that demonstrate how to track the late inspiral, plunge, and merger of a BHBH binary in vacuum [55–57]. More refined follow-up simulations of these strong-field, late phases, joined onto analytic, post-Newtonian calculations of the early inspiral epoch [58], are now capable of producing accurate gravitational waveforms for merging BHBH binaries with companions spanning a range of mass ratios and spins (see e.g. [59] and references therein).

With the problem of gravitational wave emission from a vacuum BHBH binary inspiral well in hand, it is now important to turn to the problem of electromagnetic emission from BHBH binary coalescence in an astrophysically realistic gaseous environment.

In Paper I, we considered *hot* accretion flows in which the gas is near the galaxy virial temperature and the specific angular momentum of the gas $\tilde{L}$ is less than that of a circular orbit near the horizon, $\tilde{L} \lesssim Mc$. Such flows can be

well described by the spherical Bondi, or Bondi-Hoyle-Lyttleton accretion model. In this paper, we consider flows in which the angular momentum of the gas cannot be neglected, and the accretion flow is disklike.

Disk accretion onto a BHBH binary has been studied previously in the Newtonian, geometrically thin-disk limit, both analytically [12,14,15,60–62] and numerically [8,10,11,36]. We extend this work by performing fully relativistic hydrodynamcal simulations in $3+1$ dimensions. Our treatment here is quite preliminary and meant to introduce the computational framework for more detailed and realistic simulations that we are preparing. In this paper we restrict our attention to a circumbinary disk residing in the orbital plane of two nonspinning, equal-mass, binary black holes. The black holes are initially in a quasistationary, nearly circular orbit and represent a solution to the conformal thin-sandwich (CTS) initial-value equations (see, e.g. [63–65] and references therein). The mass of the disk is assumed to be small in comparison to the total black hole mass. We explore the response of the disk to the binary on a *dynamical* time scale and thus ignore the secular motion of gas in the disk due to viscosity or turbulent magnetic fields. We treat the gas as a perfect fluid described by a Γ-law equation of state (EOS) and handle shocks by high-resolution, shock-capturing (HRSC) techniques. We study the response of the disk to tidal torques during the early and late inspiral phases, as well as during the merger and post-merger epochs. The inspiral and merger are followed by solving the BSSN field equations [50,51] with moving puncture gauge conditions [56,57]. We are particularly interested in the evolution of the hollow region in the disk about the binary [33–36] and the extent to which gas penetrates the hollow and accretes onto the black holes. We also estimate, as a perturbation, the electromagnetic emission from the disk that characterizes the inspiral and merger epochs. Our treatment is appropriate for describing the epoch following disk-binary ''decoupling,'' when the BHBH inspiral time scale is much shorter than the viscous time scale in the disk, whereby viscosity-induced inflow can be neglected. Our analysis remains valid throughout the binary merger and ringdown phases, but is no longer adequate to describe the late-time evolution when viscosity serves to drive gas into the hollow and accrete onto the merged remnant [7,12]. We briefly compare our results with another, recently published, general relativistic study [49] that treats a similar scenario, but employs different methods (e.g. different initial data and luminosity estimates) and addresses different issues.

The structure of the paper is as follows. In Sec. II we summarize the computational challenge posed by the large dynamic range associated with this problem, and we describe our approach for overcoming this challenge. In Secs. III and IV we briefly outline the basic gravitational field and matter evolution equations and their specific implementations in our numerical scheme. Here we also provide an overview of our initial data, gauge conditions, and diagnostics. In Sec. IV D, we review code tests that were performed to validate our numerical scheme. In Sec. V we describe the results of our binary BHBH merger simulations. In Sec. VI we summarize our findings, and briefly compare with previous simulations. Henceforth we adopt geometrized units and set $G = c = 1$.

II. COMPUTATIONAL CHALLENGE

Simulating realistic accretion flows is extremely challenging due to the enormous dynamic range characterizing the time and length scales in the problem. One length scale is set by the initial, total Arnowitt-Deser-Misner (ADM) mass of the binary system, M. We neglect the mass of the disk and assume that $M_{\rm disk} \ll M$. The ADM mass sets the length scale at which relativistic effects become significant. Another important length scale is the binary orbital separation a. Associated with the orbital separation is the orbital period, $t_{\rm orb} \equiv 2\pi/\Omega_{\rm bin} \approx 2\pi(a/M)^{3/2}$, where $\Omega_{\rm bin}$ is the binary orbital angular velocity.

Torques from the binary have the effect of driving matter in the vicinity of the BHBH orbit outward, creating a hollow cavity inside the inner edge of the accretion disk at $R_{\rm in} \sim 1.5 - 2a$ [33–36]. This radius is determined by the balance between viscous stresses in the disk and tidal torques from the binary [33–36], provided that the viscous time scale $t_{\rm vis} \approx (2/3)R_{\rm in}^2/\nu$ is shorter than the gravitational inspiral time scale $t_{\rm merge} \approx (5/16)a^4/M^3$. Here ν is the shear viscosity, and we assume an equal-mass binary. As the orbital separation decreases, the binary eventually enters an epoch at which $t_{\rm merge} < t_{\rm vis}$. At this point, the binary decouples from the disk [7,14,62,66]. If one assumes an α-disk with a viscosity law $\nu(R) = (2/3)\alpha P_{\rm gas}/(\rho\Omega_K)$, where ρ is the gas density and $P_{\rm gas}$ is the gas pressure, then the decoupling radius a_d is given by [7,13,62]

$$\frac{a_d}{M} \approx 126\alpha_{-1}^{-17/50} S^{-49/200} \lambda^{7/10} M_6^{2/25} (\delta_{-1}\zeta)^{17/40} \theta_{0.2}^{-17/200}, \tag{1}$$

where $\alpha = 0.1\alpha_{-1}$, $\delta = 0.1\delta_{-1}$, $S \equiv 3\pi\Sigma(a_d)\nu(a_d)/\dot{M}_{\rm Edd}$, and $\theta = 0.2\theta_{0.2}$. Here $\dot{M}_{\rm Edd} = 4\pi M m_p/(\eta\sigma_T)$ is the Eddington accretion rate, σ_T is the Thomson cross section for electron scattering, η is the radiative efficiency, $\theta < 1$ is a porosity correction factor applied to the scattering-dominated optical depth [67], and δ roughly accounts for the shortening of the viscous time scale at the disk edge where the surface density Σ is very steep [68].

Another important length scale is the characteristic size of the disk, $R_{\rm disk}$, which we define here as the radius at which the gas pressure is maximum, $R_{\rm disk} \equiv R(P_{\rm max})$. In general, $R_{\rm disk}$ depends on the details of the temperature and angular momentum profile in the disk, and is highly dependent on the particular choice of disk model. Associated

with $R_{\rm disk}$ is the orbital time scale $t_{\rm disk}$, which we define as the Keplerian orbital period $t_{\rm disk} = 2\pi(R_{\rm disk}/M)^{3/2}$.

If we assume the size of the entire disk is several $R_{\rm disk} \gg R_{\rm in}$ and use the estimate of a_d given in Eq. (1), we find that a simulation of the full inspiral from decoupling to merger would require us to resolve length scales from $\sim M$ to $\gtrsim 10^3 M$. More challenging, we must resolve time scales from M to several $t_{\rm merge} \sim 10^8 M$. Unfortunately, the latter is beyond the capability of current numerical codes. In order to circumvent this issue, we consider a disk with relatively small values of $a_d = 10M$, $R_{\rm in} \sim 15M$, and $R_{\rm disk} \sim 35M$. With these choices, the important time scales become $t_{\rm orb} = 225M$, $t_{\rm disk} = 1300M$, and $t_{\rm merge} = 1250M$. Given the wide range of gaseous environments in galactic cores, such parameters are not implausible, and we expect that qualitative features of our results can be extended to disks with larger values of a_d, $R_{\rm in}$, and $R_{\rm disk}$. Our choice allows us to study the full evolution of the system from decoupling to binary merger. We focus on the post-decoupling phase through merger, ringdown, and disk equilibration, but prior to disk inflow on viscous time scales. Accordingly, our perfect-fluid approximation will closely mimic a realistic flow during these epochs, as the viscous time scale (which may originate from MHD turbulence) is long compared to the length of our simulations.

III. BASIC EQUATIONS

Throughout this paper, we use Latin indices to denote spatial components (1–3) and Greek indices to denote spacetime components (0–3).

A. Early inspiral epoch

We define the ''early inspiral epoch'' as the phase of the binary inspiral prior to decoupling. Throughout this phase, the inspiral time scale is much longer than the orbital time scale. This fact can be exploited by neglecting the change in binary separation and employing a metric that is quasistationary in the rotating frame of the binary. This simplification provides an accurate solution for the spacetime without the computational expense of a full evolution of Einstein's field equations. We evolve the full relativistic hydrodynamics equations in this background metric over $\sim 5 t_{\rm disk}$ to enable the disk to relax to a quasistationary state. This technique thus provides astrophysically realistic initial data with which to begin evolution of the late inspiral and merger epochs (Sec. III B).

In order to use this method, we must choose a coordinate system in which the metric explicitly reflects the symmetry of the spacetime. This symmetry, describing a spacetime that is quasistationary in a frame that rotates with the orbital frequency of the binary Ω, can be constructed by employing a helical Killing vector,

$$\xi \equiv \partial_t + \Omega \partial_\phi. \tag{2}$$

For a spacetime admitting such a Killing vector, we have

$$\mathcal{L}_\xi g_{\mu\nu} = 0, \tag{3}$$

where $\mathcal{L}$ is the Lie derivative, and $g_{\mu\nu}$ is the spacetime metric.

Provided we are working in an appropriate coordinate system (i.e. one employing Killing coordinates t and ϕ), we may express the metric at any point in spacetime in terms of the metric on an initial $t = 0$ slice according to

$$g_{\mu\nu}(t, r, \theta, \phi) \doteq g_{\mu\nu}(0, r, \theta, \phi - \Omega t), \tag{4}$$

where the symbol $\doteq$ denotes that the equality holds only in a particular coordinate system. One can easily verify that the above equation satisfies Killing's equation (3).

We note that Eq. (4) is written in spherical polar coordinates, i.e. $\{x^\alpha\} = \{t, r, \theta, \phi\}$. However, Cartesian coordinates are more suitable for work in 3D, as coordinate singularities at $r = 0$ and on the polar axis are avoided. We therefore transform the spherical components of $g_{\mu\nu}$ back to the Cartesian components using the usual tensor transformation formula.

BHBH evolution employing standard puncture initial data and moving puncture gauge conditions does not result in a metric that satisfies Eq. (3) (Puncture initial data does not implement a helical Killing vector). By contrast, BHBH CTS initial data (see, e.g. [64]) are specifically constructed to satisfy this equation: CTS initial data impose the condition that the spacetime in the rotating frame is stationary (see [65] for discussion and references). This condition is valid, approximately, whenever the binary companions are sufficiently well separated that the inspiral time scale is much longer than the orbital time scale. In this quasistationary early inspiral regime we can employ CTS initial data and CTS lapse and shift functions to evolve the metric via a simple coordinate rotation in lieu of integrating the Einstein field equations. We can then evolve the disk by integrating the hydrodynamic equations for the fluid in this background spacetime.

CTS initial data contains excised interiors. We follow the technique outlined in [69] and fill the excised region inside the BH interiors with smoothly extrapolated ''junk'' (i.e., constraint-violating) data. This treatment is valid because the interior regions are causally disconnected from the exterior spacetime.

B. Late inspiral and merger epochs

We evolve both the metric and hydrodynamic equations during the late inspiral and merger epochs. Our basic gravitational field and relativistic hydrodynamics equations are discussed in [51,70], where their numerical implementation is described and detailed code tests are summarized. Here, we briefly review these equations and their implementation.

We write the spacetime metric in the standard $3 + 1$ form,

$$ds^2 = -\alpha^2 dt^2 + \gamma_{ij}(dx^i + \beta^i dt)(dx^j + \beta^j dt), \quad (5)$$

where α, β^i, and γ_{ij} are the lapse, shift, and spatial metric, respectively. The extrinsic curvature K_{ij} is given by

$$(\partial_t - \mathcal{L}_\beta)\gamma_{ij} = -2\alpha K_{ij}, \quad (6)$$

where $\mathcal{L}_\beta$ is the Lie derivative with respect to β^i. We evolve γ_{ij} and K_{ij} using the BSSN formulation [50,51]. The fundamental variables for BSSN evolution are

$$\phi \equiv \frac{1}{12}\ln[\det(\gamma_{ij})], \quad (7)$$

$$\tilde{\gamma}_{ij} \equiv e^{-4\phi}\gamma_{ij}, \quad (8)$$

$$K \equiv \gamma^{ij}K_{ij}, \quad (9)$$

$$\tilde{A}_{ij} \equiv e^{-4\phi}\left(K_{ij} - \frac{1}{3}\gamma_{ij}K\right), \quad (10)$$

$$\tilde{\Gamma}^i \equiv -\tilde{\gamma}^{ij}{}_{,j}. \quad (11)$$

The evolution and constraint equations for these fields are summarized in [50,51]. We assume in this paper that the mass of the gas is negligible compared to the mass of the BHs, thus we do not include matter source terms in our metric evolution equations.

Adding Kreiss-Oliger dissipation to the BSSN evolution equations outside the BH can reduce high-frequency numerical noise associated with adaptive mesh refinement (AMR) refinement interfaces [57]. We use this technique here and have found it useful in reducing Hamiltonian and momentum constraint violations.

We adopt the standard moving puncture gauge conditions: an advective "1 + log" slicing condition for the lapse and a "Gamma-freezing" condition for the shift [71]. Thus we have

$$\partial_0\alpha = -2\alpha K, \quad (12)$$

$$\partial_0\beta^i = (3/4)B^i, \quad (13)$$

$$\partial_0 B^i = \partial_0\tilde{\Gamma}^i - \eta B^i, \quad (14)$$

where $\partial_0 = \partial_t - \beta^j\partial_j$. The η parameter is set to $0.5/M$ in all simulations.

C. Evolution of hydrodynamic fields

The fundamental matter variables are the rest-mass density ρ_0, specific internal energy ϵ, pressure P, and four-velocity u^μ. The stress-energy tensor for an ideal gas is given by

$$T_{\mu\nu} = \rho_0 h u_\mu u_\nu + P g_{\mu\nu},$$

where $h = 1 + \epsilon + P/\rho_0$ is the specific enthalpy. We evolve the "conservative" variables ρ_*, $\tilde{S}_i$, and $\tilde{\tau}$. They are defined as

$$\rho_* = -\sqrt{\gamma}\rho_0 n_\mu u^\mu, \quad (15)$$

$$\tilde{S}_i = \sqrt{\gamma}T_{\mu\nu}n^\mu\gamma^\nu_i, \quad (16)$$

$$\tilde{\tau} = \sqrt{\gamma}T_{\mu\nu}n^\mu n^\nu - \rho_*. \quad (17)$$

Here $n^\alpha = (\alpha^{-1}, -\alpha^{-1}\beta^i)$ is the timelike unit vector normal to the $t =$ constant time slices. Evolution equations are given by Eqs. (34), (36), and (38) of [70]:

$$\partial_t\rho_* + \partial_j(\rho_* v^j) = 0, \quad (18)$$

$$\partial_t\tilde{S}_i + \partial_j(\alpha\sqrt{\gamma}T^j_i) = \tfrac{1}{2}\alpha\sqrt{\gamma}T^{\alpha\beta}\partial_i g_{\alpha\beta}, \quad (19)$$

$$\partial_t\tilde{\tau} + \partial_i(\alpha^2\sqrt{\gamma}T^{0i} - \rho_* v^i) = s, \quad (20)$$

where $\gamma \equiv \det(\gamma_{ij}) = e^{12\phi}$ and $v^i \equiv u^i/u^0$ is the fluid's 3-velocity. The energy source term s is given by

$$s = -\alpha\sqrt{\gamma}T^{\mu\nu}\nabla_\nu n_\mu = \alpha\sqrt{\gamma}[(T^{00}\beta^i\beta^j + 2T^{0i}\beta^j + T^{ij})K_{ij} - (T^{00}\beta^i + T^{0i})\partial_i\alpha]. \quad (21)$$

D. Equation of state

To complete the system of equations, we must specify an EOS. While our code can handle any EOS of the form $P = P(\rho_0, \epsilon)$, we adopt a Γ-law EOS,

$$P = (\Gamma - 1)\rho_0\epsilon. \quad (22)$$

We perform simulations with $\Gamma = 4/3$, $5/3$, and 1.1. By varying Γ we effectively examine gas flow under a full range of conditions. We choose $\Gamma = 5/3$ as our canonical case. The choice of $\Gamma = 1.1$ approximates an isothermal gas (we have chosen $\Gamma = 1.1$ rather than $\Gamma = 1$ in order to retain the Γ-law form of the EOS while still approximating isothermality). At $t = 0$, we take the EOS to be isentropic, with $P = K\rho_0^\Gamma$, where $K =$ constant. Throughout this paper, we define temperature by

$$P = 2nkT, \quad (23)$$

appropriate for pure ionized hydrogen.

IV. NUMERICAL METHODS

A. Disk initial data

For our disk initial data, we use the equilibrium solution for a stationary disk around a *single* Kerr BH derived by Chakrabarti *et al.* [72] and summarized in [73]. We take this disk as initial data for a binary BHBH, placing the inner boundary of the disk well outside the BHBH orbital radius. Though no longer stationary, the initial disk settles

TABLE I. Parameters for BHBH simulations.

Case	Epoch[a]	Orientation	Γ	H/R[b]
A1	early inspiral	prograde	5/3	0.11
A2			4/3	0.08
A3			[c]1.1	0.03
A4		retrograde	4/3	0.08
B1	late inspiral	prograde	5/3	0.14
B2	and merger		4/3	0.11
B3			[c]1.1	0.06
B4		retrograde	4/3	0.11

[a]Initial binary separation $a/M = 10$.
[b]H is the scale height of the disk at $R = R_{\rm disk}$ (pressure max), measured at $t = 0$ for case A runs and at $t = t_{\rm merge}$ for case B runs.
[c]Approximately isothermal.

down to quasistationary equilibrium as the binary rotates, apart from low amplitude spiral density waves induced by the time-varying tidal torque. For completeness, we provide a brief summary of the construction of disk initial data in Appendix A.

For our fiducial equation of state, $\Gamma = 5/3$, the resulting outer disk radius is $R_{\rm out} \approx 65M$ and the disk scale height at $R_{\rm disk}$ is $H/R = 0.11$ (see Table I for more details). Here H is defined as the height above the equatorial plane where the pressure falls to $1/e$ its value on the equatorial plane at the radius of maximum pressure. For binary BHs, the disk is approximately stationary if $R_{\rm in} \gg a$. Initially, we take $R_{\rm in}/a = 1.5$. We find that the disk relaxes to a near quasistationary state after a time $\sim 4t_{\rm disk}$.

B. Evolution of metric and matter

We evolve the BSSN field equations with fourth-order accurate, centered, finite-difference stencils, except on shift advection terms, where we use fourth-order accurate upwind stencils. We apply Sommerfeld outgoing wave boundary conditions to all BSSN fields. Our code is embedded in the Cactus parallelization framework [74], and our fourth-order Runge-Kutta time-stepping is managed by the MoL (method of lines) thorn, with a Courant-Friedrichs-Lewy factor set to 0.5 in all BHBH simulations. We use the Carpet [75] infrastructure to implement the moving-box AMR. In all AMR simulations presented here, we use second-order temporal prolongation, coupled with fifth-order spatial prolongation. The apparent horizon of the BH is computed with the AHFINDERDIRECT Cactus thorn [76].

We write the general-relativistic hydrodynamics equations in conservative form. They are evolved by an HRSC technique [70] that employs the piecewise parabolic reconstruction (PPM) scheme [77] coupled to the Harten, Lax, and van Leer (HLL) approximate Riemann solver [78]. The adopted hydrodynamic scheme is second-order accurate for smooth flows, and first-order accurate when discontinuities (e.g. shocks) arise. Throughout the evolution, we impose limits on the pressure to prevent spurious heating and negative values of the internal energy ϵ. Specifically, we require $P_{\rm min} \le P \le P_{\rm max}$ inside the horizon, where $P_{\rm max} = 10K\rho_0^\Gamma$ and $P_{\rm min} = K\rho_0^\Gamma/2$. Whenever P exceeds $P_{\rm max}$ or drops below $P_{\rm min}$, we reset P to $P_{\rm max}$ or $P_{\rm min}$, respectively. We check that this fix is applied only inside the apparent horizon, which is causally disconnected from the rest of the grid.

At each time step, we need to recover the "primitive variables" ρ_0, P, and v^i from the "conservative variables" ρ_*, $\tilde{\tau}$, and $\tilde{S}_i$. We perform the inversion as specified in Eqs. (57)–(62) of [70], but with a slightly modified analytic quartic solver from the GNU Scientific Library that outputs only the real roots. We use the same technique as in [79] to ensure that the values of $\tilde{S}_i$ and $\tilde{\tau}$ yield physically valid primitive variables, except we reset $\tilde{\tau}$ to $10^{-10}\tilde{\tau}_{0,\rm max}$ (where $\tilde{\tau}_{0,\rm max}$ is the maximum value of $\tilde{\tau}$ initially) when either $\tilde{S}_i$ or $\tilde{\tau}$ is unphysical (i.e., violate one of the inequalities (34) or (35) in [79]). The restrictions usually apply only to the region near the puncture inside the horizon.

For each of our calculations, we set our outer boundary at $128M$ and use 8 AMR refinement levels. The maximum resolution near each BH is $\delta x/M = 0.03125$. For our single BH test calculations, we place our outer boundary at $128M$ and use 6 AMR refinement levels. For these cases, the highest resolution near the BH is $\delta x/M = 0.0625$.

We model the emission of electromagnetic radiation by treating this radiation loss as a perturbation, and neglect its influence on the hydrodynamic flow, as well as any deviation from adiabaticity that it induces.

C. Diagnostics

1. Surface density

In order to track the global evolution of disk structure and compare with other disk calculations, it is useful to define the surface density Σ. Following [80], we define

$$\Sigma(R, \phi) = \int_{z\ge 0} \rho_0 u^t \sqrt{-g} dz, \tag{24}$$

where $R \equiv \sqrt{x^2 + y^2}$ (R will always be the cylindrical radius in this paper, while r will always be the spherical polar radius). We also report the angle-averaged surface density $\langle\Sigma(R)\rangle$ where

$$\langle\Sigma\rangle \equiv \frac{1}{2\pi}\int_0^{2\pi} \Sigma d\phi. \tag{25}$$

2. Flux diagnostics

To derive meaningful flux diagnostics we must identify the conserved currents. Details of this derivation are given in Appendix A of [16]. To summarize, consider a 3D region Σ_t which lies between two world tubes F and L on a time slice $t = \text{const}$. Let F be defined by $h(t, x, y, z) = 0$, and L be defined by $l(t, x, y, z) = 0$. In [16], this region is depicted as the lower shaded region in

Fig. 24. For the purposes of this paper, we let F be the world tube defined by the apparent horizon(s), and L be the world tube defined by a sphere of constant coordinate radius centered at the origin. Of course the surfaces could be chosen to take on other shapes as well.

3. Conserved quantities

Now consider a conserved current, j^μ which satisfies

$$\nabla_\mu j^\mu = 0. \tag{26}$$

Then it can be shown that (see e.g. Appendix A of [16])

$$\dot{q} \equiv \frac{dq}{dt} = -\mathcal{F}_F + \mathcal{F}_L, \tag{27}$$

where

$$q(t) = \int_{\Sigma_t} j^\mu d^3\Pi_\mu \tag{28}$$

$$= \int_{\Sigma_t} j^t \sqrt{-g} d^3x, \tag{29}$$

$$\mathcal{F}_F = -\int_F \sqrt{-g'} j^h da db, \tag{30}$$

$$\mathcal{F}_L = -\int_L \sqrt{-g'} j^l da db. \tag{31}$$

Here g' is the determinant of the metric in the (t, h, a, b) or (t, l, a, b) coordinate systems. In the above example, $\mathcal{F}_F$ is the flux of q across the horizon(s), while $\mathcal{F}_L$ is the flux of q across the outer sphere.

4. Freedom in coordinate choice

These fluxes are independent of any changes in coordinates that leave the slicing intact. Equivalently, we may alter the shift without affecting the flux, but the lapse must be kept the same. We can rewrite these fluxes in any other coordinate system (t, x, y, z) which preserves the same slicing. While a and b can be any two coordinates on the surface, we label them here as θ and ϕ for convenience, as this is done in our actual numerical calculations,

$$\mathcal{F}_F = -\int_F \sqrt{-g} \det\left|\frac{\partial(x, y, z)}{\partial(h, \theta, \phi)}\right| j^\mu \partial_\mu h d\theta d\phi, \tag{32}$$

$$\mathcal{F}_L = -\int_L \sqrt{-g} \det\left|\frac{\partial(x, y, z)}{\partial(l, \theta, \phi)}\right| j^\mu \partial_\mu l d\theta d\phi. \tag{33}$$

5. Rest-mass conservation

Rest-mass conservation, $\nabla_\mu(\rho_0 u^\mu) = 0$, corresponds to $j^\mu = \rho_0 u^\mu$. If we now define

$$M_0 \equiv \int_{\Sigma_t} \sqrt{-g} \rho_0 u^0 d^3x = \int_{\Sigma_t} \rho_* d^3x, \tag{34}$$

$$\mathcal{F}_F^{(M)} \equiv -\int_F \sqrt{-g} \det\left|\frac{\partial(x, y, z)}{\partial(h, \theta, \phi)}\right| \rho_0 u^\mu h_{,\mu} d\theta d\phi, \tag{35}$$

$$\mathcal{F}_L^{(M)} \equiv -\int_L \sqrt{-g} \det\left|\frac{\partial(x, y, z)}{\partial(l, \theta, \phi)}\right| \rho_0 u^\mu l_{,\mu} d\theta d\phi, \tag{36}$$

then we may integrate Eq. (27) in time to derive the following rest-mass conservation law

$$\left(M_0(t) + \int_{t_i}^t dt(\mathcal{F}_F^{(M)} - \mathcal{F}_L^{(M)})\right) \Big/ M_{0,i} = 1, \tag{37}$$

where $M_{0,i}$ is the rest mass between the horizons and the surface L at $t = 0$. Equivalently, we can define the rest-mass accretion rate

$$\dot{M}_0 \equiv -\mathcal{F}_F^{(M)} + \mathcal{F}_L^{(M)}. \tag{38}$$

6. $E - \Omega J$ conservation

We employ the helical Killing vector defined in Eq. (2) to construct another conserved current,

$$j^\mu \equiv \xi_\nu T^{\mu\nu} = T^\mu{}_t + \Omega T^\mu{}_\phi. \tag{39}$$

We now define the following quantities

$$E(t) \equiv -\int_{\Sigma_t} \sqrt{-g} T^t{}_t d^3x, \tag{40}$$

$$J(t) \equiv \int_{\Sigma_t} \sqrt{-g} T^t{}_\phi d^3x, \tag{41}$$

$$\mathcal{F}_F^{(E)} \equiv \int_F \sqrt{-g} \det\left|\frac{\partial(x, y, z)}{\partial(h, \theta, \phi)}\right| T^\mu{}_t h_{,\mu} d\theta d\phi, \tag{42}$$

$$\mathcal{F}_L^{(E)} \equiv \int_L \sqrt{-g} \det\left|\frac{\partial(x, y, z)}{\partial(l, \theta, \phi)}\right| T^\mu{}_t l_{,\mu} d\theta d\phi, \tag{43}$$

$$\mathcal{F}_F^{(J)} \equiv -\int_F \sqrt{-g} \det\left|\frac{\partial(x, y, z)}{\partial(h, \theta, \phi)}\right| T^\mu{}_\phi h_{,\mu} d\theta d\phi, \tag{44}$$

$$\mathcal{F}_L^{(J)} \equiv -\int_L \sqrt{-g} \det\left|\frac{\partial(x, y, z)}{\partial(l, \theta, \phi)}\right| T^\mu{}_\phi l_{,\mu} d\theta d\phi, \tag{45}$$

and we see that Eqs. (27) and (39) give

$$\dot{E} - \Omega \dot{J} = -(\mathcal{F}_F^{(E)} - \Omega \mathcal{F}_F^{(J)}) + (\mathcal{F}_L^{(E)} - \Omega \mathcal{F}_L^{(J)}), \tag{46}$$

for spacetimes possessing a helical Killing vector. Again, we may integrate in time to derive another conservation law

$$E(t) - \Omega J(t) + \int_{t_i}^t dt(\mathcal{F}_F^{(E)} - \Omega \mathcal{F}_F^{(J)}) - \int_{t_i}^t dt(\mathcal{F}_L^{(E)} - \Omega \mathcal{F}_L^{(J)}) = E(t_i) - \Omega J(t_i). \tag{47}$$

7. Spiral density wave diagnostics

In our simulations, we use our CTS metric and Eq. (4) to ensure that our disk models exhibit quasistationary behavior before we begin the binary inspiral. Such quasistationary configurations are interesting in their own right, as they lend insight into any accretion flow onto a binary before merger. A key feature of this flow is the presence of spiral density waves in the inner disk cavity. Following [36], we highlight the existence of these density waves by calculating the surface density fluctuation $\delta\Sigma$, defined by

$$\delta\Sigma \equiv \frac{\Sigma - \langle\Sigma\rangle}{\langle\Sigma\rangle}. \tag{48}$$

We also define the torque density, dT/dR, for comparison with analytic models and other simulations,

$$\frac{dT}{dR} = \int \sqrt{-g} T^{\mu}{}_{\nu} \nabla_{\mu} \phi^{\nu} R dz d\phi, \tag{49}$$

where $\phi^{\mu} \equiv (\partial_{\phi})^{\mu}$, which gives $\phi^{\mu} = (0, -y, x, 0)$ in Cartesian coordinates. Details of the derivation of Eq. (49) are given in Appendix B.

8. Luminosity diagnostics

In order to study the electromagnetic emission from our disk evolutions, we estimate the luminosity due to thermal bremmstrahlung and nonthermal synchrotron emission using the approximations described in [16]. For synchrotron emission, we assume the presence of a small-scale, turbulent B field whose magnitude is approximated by setting $P = \beta P_M \equiv \beta B^2/(8\pi)$. We thus assume that the magnetic pressure is some fraction $1/\beta$ of its equipartition value. Simulations of magnetized accretion flows have demonstrated that the magnetic fields do not typically reach their full equipartition value [81]. We have chosen $\beta = 10$ to account for this. We also assume that the radiation propagates through an optically thin gas, and we neglect the roles of radiation pressure and radiative cooling on the hydrodynamic evolution. While an accurate estimation of the electromagnetic emission requires a full solution to the radiative transfer problem, this crude method can provide a reasonable estimate of the magnitude of the emission under suitable conditions.

D. Code tests

Our HRSC general-relativistic hydrodynamic code has been thoroughly tested by passing a robust suite of tests. These tests include maintaining stable rotating stars in stationary equilibrium, reproducing the exact Oppenheimer-Snyder solution for collapse to a BH, and reproducing analytic solutions for relativistic shocks and spherical Bondi accretion onto isolated BHs [70]. Our code has also been used to simulate the collapse of very massive, rotating stars to black holes [82]; merging BHBH binaries [69], BHNS binaries [79,83], and relativistic hydrodynamic matter in the presence of puncture black holes [84]. Recently, our code has been generalized to incorporate (optically thick) radiation transport and its feedback on fluids in dynamical spacetimes [85].

Most of the above tests and simulations were performed on grids with uniform spacing. In some of the simulations, we utilized the multiple-transition fisheye transformation [86] so that a uniform computational grid spacing corresponds to physical coordinates with spatially varying resolution. Recently, we have modified our code so that we can use the moving-box AMR infrastructure provided by Carpet [75]. To test our new code, we have performed shock-tube tests and 3 + 1 simulations of linear gravitational waves, single stationary and boosted puncture BHs, puncture BHBH binaries, and rapidly and differentially rotating relativistic stars. Our AMR code has also been used to perform simulations of BHNS mergers [83], binary Bondi, and binary Bondi-Hoyle-Lyttleton accretion [16].

All of our 3 + 1 AMR code tests were performed assuming equatorial symmetry (i.e., symmetry about the $z = 0$ orbital plane), which we assume in all evolutions presented in this paper. We have checked that our AMR code is able to accurately maintain a stable equilibrium disk around a single BH, as demonstrated in Fig. 1. For this test, we use the same disk initial data as run A1 in Table I, except that we set the background metric to be that of a single Schwarzchild BH at the origin. As we describe in Sec. IV A, such a disk is an equilibrium solution and is expected to maintain its initial profile.

We have also checked that the conservations laws in Eqs. (37) and (47) are satisfied in a quasistationary, binary spacetime, as described in Sec. IV C. In Fig. 2, the dashed red curve shows the left-hand side of Eq. (37), with the world tube L chosen to correspond to a sphere centered at the origin with a radius $r_L = 25M$. For comparison, we also plot $M_0(t)/M_{0,i}$ with the solid red curve. The data are from run A2, in which we impose a helical Killing vector to solve for the metric as described in Sec. III A, while

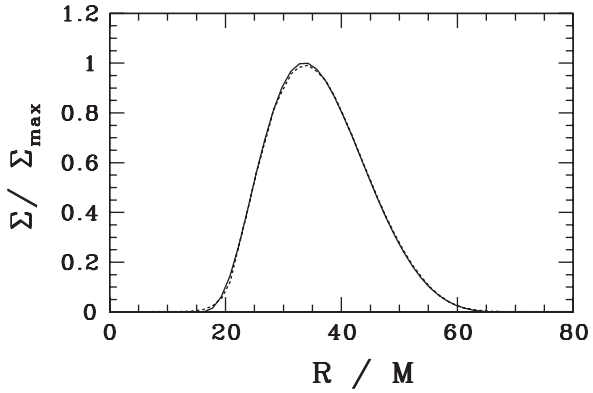

FIG. 1. Surface density profiles at $t = 0$ (solid line) and $t \approx t_{\rm disk}$ (dotted line), where $t_{\rm disk}$ is the Keplerian period at the radius of maximum pressure. Overlap indicates that disk accurately maintains equilibrium configuration over this time scale.

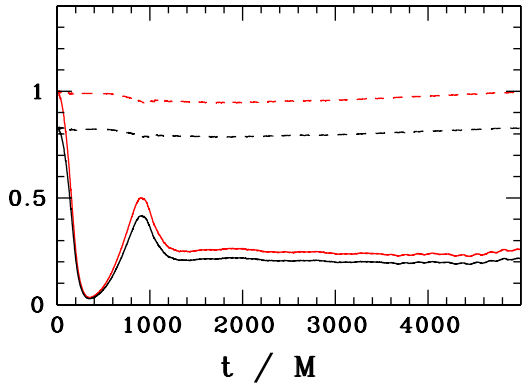

FIG. 2 (color online). Plots demonstrating the accurate maintenance of conserved quantities. Rest mass $M_0(t)/M_{0,i} + \int dt(\mathcal{F}_F^{(M)} - \mathcal{F}_L^{(M)})/M_{0,i}$ (dashed red line) maintains its initial value accurately when compared to $M_0/M_{0,i}$ (solid red). Similarly, the conserved quantity $(E(t) - \Omega J(t) + \int dt(\mathcal{F}_F^{(E)} - \Omega\mathcal{F}_F^{(J)}) - \int dt(\mathcal{F}_L^{(E)} - \Omega\mathcal{F}_L^{(J)}))/M_{0,i}$ (dashed black line) maintains its initial value accurately when compared to $(E(t) - \Omega J(t))/M_{0,i}$ (solid black line).

evolving the hydrodynamics using Eqs. (18)–(20). We find that Eq. (37) is well satisfied, indicating that our code is conserving rest mass correctly. Similarly, the dashed black line shows the left-hand side of Eq. (47), normalized by $M_{0,i}$, while the solid black line shows $(E(t) - \Omega J(t))/M_{0,i}$ for comparison. Again, we see that our code is conserving $E - \Omega J$ correctly.

V. RESULTS

As discussed in Sec. III, we separate each of our simulations into two phases. We first perform early inspiral epoch simulations in which we employ the quasistationary CTS metric while keeping the BH separation constant. This allows the disk to relax to a reliable quasistationary state. Upon achieving this state, we begin our late inspiral and merger epochs simulations in which we evolve the metric in full GR, allowing the BHs to inspiral and merge. Parameters for each of these disk runs are given in Table I.

Equatorial snapshots from our simulations with $\Gamma = 5/3$ can be seen in Fig. 3, while meridional snapshots are shown in Fig. 4. The first two snapshots are from the early inspiral epoch calculations, while the second two snapshots are from the late inspiral and merger epochs calculations. We do not show snapshots for other equations of state here, as the accretion flow is qualitatively similar. Important results from simulations with other equations of state are reported in Table II.

A. Early inspiral epoch

While the formulation outlined in Sec. IVA provides stable equilibrium disk initial data for a *single* BH, torques from the *binary* disrupt this equilibrium. Thus, it is important to allow the gas to relax to a quasistationary state before beginning the BH inspiral. We allow this relaxation to occur over $\sim 5t_{\rm disk}$, where $t_{\rm disk} \approx 1300M$. At this time, we find that $\dot{M}_0$, $L_{\rm syn}$, and $L_{\rm brem}$ oscillate around roughly constant values, and there is little evolution in surface density profiles. Here $L_{\rm syn}$ and $L_{\rm brem}$ refer to synchrotron and bremsstrahlung luminosity, respectively.

During the relaxation process, the changes in the matter profiles are due to the presence of binary torques. These torques cause a disruption of the inner edge of the disk, allowing some gas to fall onto the BHs. Infalling gas forms spiral waves and shocks which heat the gas near the BHs. In the absence of shock heating, the disk would behave adiabatically, and the internal energy density would be given by its polytropic value,

$$\rho_0 \epsilon_{ad} = K\rho_0^\Gamma/(\Gamma - 1). \tag{50}$$

Thus, shock heating may be measured by computing the enhancement in the internal energy density above its adiabatic value and integrating over the disk. We therefore compute

$$E_{\rm int} = \int_{V_d} \sqrt{-g}\rho_0 u^t \epsilon d^3x, \tag{51}$$

and

$$E_{{\rm int},ad} = \int_{V_d} \sqrt{-g}\rho_0 u^t \epsilon_{ad} d^3x. \tag{52}$$

Here the integral is over V_d, which is the volume between $r = 10M$ and the outer boundary of the computational domain at $128M$. This allows us to compute $\Delta E_{\rm int}$ in the bulk of the disk, ignoring the gas near the BHs. In Fig. 5, we plot $\Delta E_{\rm int}/E_{{\rm int},ad}$ vs time during the relaxation of the gas, where $\Delta E_{\rm int} \equiv (E_{\rm int} - E_{{\rm int},ad})$. We find that $\Delta E_{\rm int}/E_{{\rm int},ad}$ increases monotonically over the course of the relaxation process, leveling off to a constant value of $\approx 5 \times 10^{-4}$ as the disk reaches a quasistationary state. Because $\Delta E_{\rm int}/E_{{\rm int},ad} \ll 1$, we conclude that shock heating does not play a significant role in altering the bulk disk profile during this process.

In order to get a sense of the change in the disk profile from the initial data, we plot angle-averaged surface density profiles (see Fig. 6). In each case, the torque from the binary has the overall effect of pushing matter outward. However, the effect of the torques diminishes once the disk matter has moved outward and a quasistationary state is achieved after $t \sim 5t_{\rm disk}$.

In Fig. 3, we plot snapshots of density contours for case A1. We see that the disk cavity, which initially extends to $R = 15M$, becomes partially filled, with a clear spiral structure, at small radii $R \lesssim 2a = 20M$ for each of the prograde cases. A similar spiral arm structure extending inside the disk cavity has been seen in Newtonian simulations (cf. [36,87,88]). In the retrograde case (A4), this structure is largely absent. This point is further emphasized

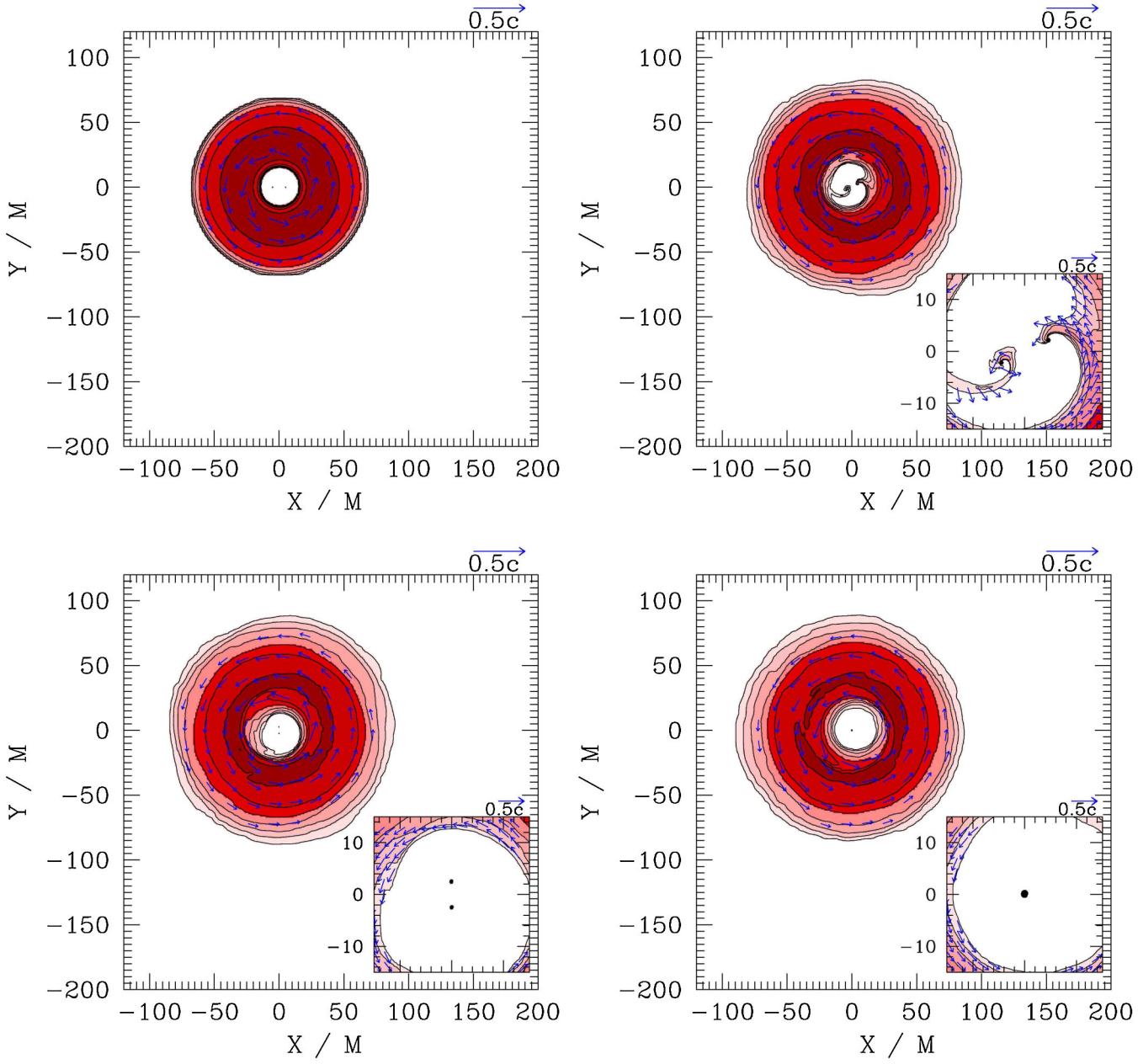

FIG. 3 (color online). Snapshots of rest-mass density ρ_0 contours in the orbital plane for cases with $\Gamma = 5/3$. Density contours are plotted at $\rho_0/\rho_{0,\max} = 10^{-2.75+0.5j}$ ($j = 1, 2, \ldots, 6$). Contours of highest density are shown with darker shading and are near the BHs. Blue arrows denote velocity vectors. The apparent horizon interior is marked by a filled black circle. The top left frame is the initial data from the early inspiral epoch, the top right frame is the relaxed, quasistationary disk, which serves as initial data for the late inspiral and merger epochs at $t \approx t_{\rm merge} - 1250M$. The bottom left frame is the data from the late inspiral and merger epochs run at $t \sim t_{\rm merge} - 50M$, while the bottom left frame is the data from the late inspiral and merger epochs at $t \approx t_{\rm merge} + t_{\rm disk}$.

by comparing the surface density fluctuation $\Delta\Sigma \equiv (\Sigma - \langle\Sigma\rangle)/\langle\Sigma\rangle$ between the prograde case A2 and the retrograde case A4 (see Figs. 7 and 8). Following [36], we compute this quantity in a rotating frame in which the binary is stationary, and average over several $t_{\rm orb}$. In Fig. 7, we clearly see two strong spiral arms emanating from each BH and extending throughout the cavity region. However, unlike the results of the 2D, thin-disk simulations presented in [36], we do not see spiral density waves extending into the bulk of the disk. We attribute this to the fact that our 3d disks are thicker, which allows waves that are initially propagating in the radial direction to be deflected in the vertical direction, disrupting the spiral density wave structure. Such effects have been demonstrated even for geometrically thin disks in which density and temperature are stratified in the z direction [89,90].

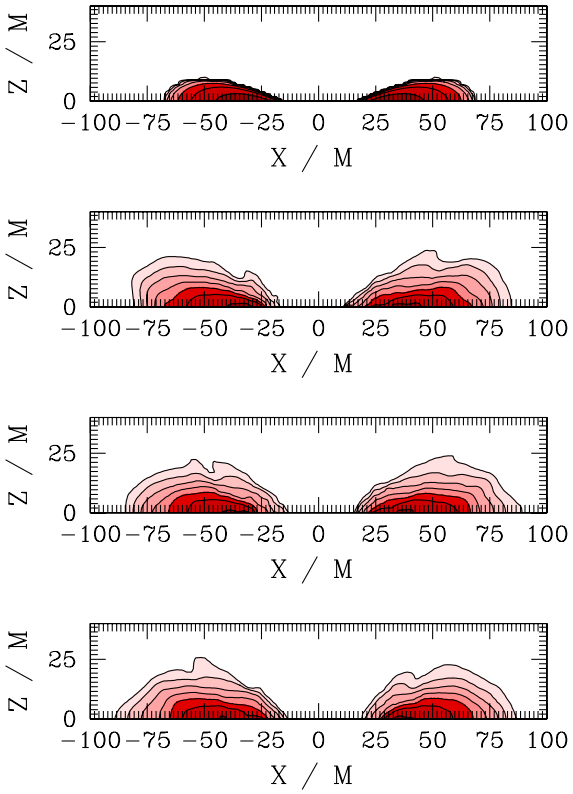

FIG. 4 (color online). Snapshots of rest-mass density ρ_0 contours in the meridional plane for cases with $\Gamma = 5/3$. Density contours are plotted at $\rho_0/\rho_{0,\max} = 10^{-2.75+0.5j}$ ($j = 1, 2, \ldots, 6$). Contours of highest density are near the BHs. The top frame is the initial data for the early inspiral epoch; the second frame is the relaxed, quasistationary disk that serves as initial data for the late inspiral and merger epochs; the third frame is the data from the late inspiral and merger epochs at $t \sim t_{\rm merge} - 50M$; the bottom frame is the data from the late inpiral and merger epochs at $t \approx t_{\rm merge} + t_{\rm disk}$.

The structure of the spiral density waves observed near $R_{\rm in}$ is roughly consistent with the theoretical Newtonian picture of a wave that is excited by the binary torques at the outermost Lindblad resonance at $R_2 = (3/2)^{2/3}a$ with orbital resonance $\Omega_{\rm bin}$:$\Omega = 3$:2 (initially, $R_2 = 0.87R_{\rm in}$). We demonstrate this by computing the angle-averaged torque density as described in Sec. IV C 7 and comparing with the (Newtonian) analytic prediction given in Eq. (31) of [36],

$$\frac{dT}{dR} \approx \frac{49}{288}\pi^2\Sigma(R_2)\Omega_{\rm bin}^2\frac{a^4}{\lambda_2}\,{\rm Ai}\left(\frac{R_2 - R}{\lambda_2}\right), \qquad (53)$$

where $\lambda_2 = 2^{-2/3}(H/R)^{2/3}a$. Based on numerical data from run A1 at $t \gtrsim 5t_{\rm disk}$, we choose $\Sigma(R_2) = 4 \times 10^{-4}\Sigma_0$ and $H/R = 0.3$, where Σ_0 is the initial maximum surface density and H/R is measured at R_2. As we show in Fig. 9, we find very good agreement with the analytic prediction out to $R/a \approx 2.2$, but break down at larger radii. This breakdown is not unexpected, as we have argued above that spiral density waves do not extend into the bulk of the disk as a result of the thickness of our 3d disks.

For the retrograde case (A4), we find that the spiral density waves are largely absent, as shown in Figs. 8 and 10. This is expected, as the Lindblad resonance does not exist when the angular momentum of the disk and the binary are antialigned.

B. Late inspiral and merger epochs

Having allowed the disk to relax to a quasistationary state, we turn to the fully relativistic evolution of metric and matter fields in order to investigate variations in electromagnetic luminosity over the course of the inspiral and merger. Our calculations in this epoch apply to the decoupling phase of binary inspiral, through merger, but before appreciable gas fills the hollow due to viscosity. We again consider the prograde cases with $\Gamma = 4/3$ (B1), $\Gamma = 5/3$ (B2), and $\Gamma = 1.1$ (B3), as well as the retrograde case with $\Gamma = 4/3$ (B4). In each case, we use the relaxed data from the end of the corresponding quasistationary metric run as initial data.

As the binary inspiral proceeds and the separation shrinks, the torques due to the binary are diminished. As

TABLE II. Electromagnetic emission at beginning of late inspiral and merger epoch and shortly before merger.

Case	Time	$\dot{M}_0/(\rho_{\max}M^2)$ [a]	L_{ff}/L_{46} [b]	$L_{\rm syn}/L_{46}$	$h\nu_{ff}$ [$(1+z)^{-1}$ MeV] [c]	$h\nu_{\rm syn}$ [$(1+z)^{-1}n_{12}^{1/2}\beta_1^{-1/2}$ eV] [d]
B1	$t_{\rm merge} - 1250M$	0.02	0.65	$1.2\beta_1^{-1}$	0.3	2.5
B2		0.003	0.16	$0.05\beta_1^{-1}$	0.2	0.6
B3		0.0005	0.003	$2 \times 10^{-5}\beta_1^{-1}$	0.08	0.01
B4		0.01	0.15	$0.5\beta_1^{-1}$	0.2	1.6
B1	$t_{\rm merge} - 50M$	0.0003	0.60	$0.3\beta_1^{-1}$	0.3	1.7
B2		0.0005	0.14	$0.008\beta_1^{-1}$	0.2	1.5
B3		0.0001	0.002	$2.0 \times 10^{-6}\beta_1^{-1}$	0.08	1.7
B4		0.0005	0.13	$0.0002\beta_1^{-1}$	0.2	1.4

[a] $\rho_{\max}M^2 = 0.2n_{12}M_8^2M_\odot\ {\rm yr}^{-1}$, $n_{12} \equiv n/10^{12}\ {\rm cm}^{-3}$, $M_8 \equiv M/10^8M_\odot$.
[b] $L_{46} = 10^{46}n_{12}^2M_8^3\ {\rm erg\,s}^{-1}$.
[c] $h\nu_{ff} = kT_{\rm disk}$.
[d] $\beta_1 \equiv \beta/10$, $\beta \equiv 8\pi P/B^2$.

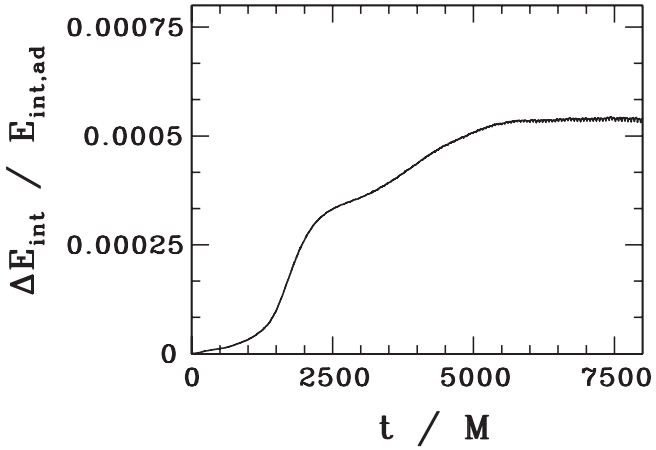

FIG. 5. Time evolution of $\Delta E_{\rm int}/E_{{\rm int},ad}$ for run A2.

a result, we find that the spiral density waves visible when $a/M = 10$ have largely disappeared by the time of merger and remain absent after the merger. This is evident in the bottom left and right frames of Fig. 3, which show snapshots of the density in the equatorial plane $\sim 50M$ before merger, and $\sim 1 t_{\rm disk}$ after merger. This effect is also illustrated by the evolution of $\dot{M}_0$, $L_{\rm brem}$, and $L_{\rm syn}$ in Fig. 11. Here, we have computed the luminosity assuming a fiducial value of $n_{\rm disk} = 10^{12}$ cm^{-3}, where $n_{\rm disk}$ is the baryon number density at $R_{\rm disk}$. This value is consistent with density estimates for a typical AGN derived from the Shakura-Sunyaev disk model [91–93], albeit in a radiation-dominated, geometrically thin regime. However, because there are large variations in the gas densities in galactic cores, we provide density scalings for our results. Because the position of the $m = 2$ outermost Lindblad resonance is approximately given by $R_2 \approx (3/2)^{2/3} a$, we see that as the

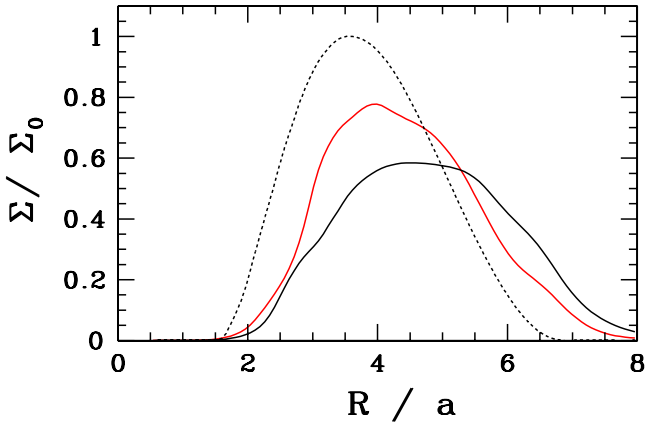

FIG. 6 (color online). Surface density profiles of the $\Gamma = 5/3$ disk as a function of radius. The dashed black curve is the initial disk density prole; the solid red one is the surface density prole when the disk has reached a quasistationary configuration after $t \gtrsim 5 t_{\rm disk}$, averaged over $\sim 2 t_{\rm orb}$. The solid black curve is the density profile following the merger, averaged over $\sim 2 t_{\rm orb}$. Σ_0 is the initial maximum surface density.

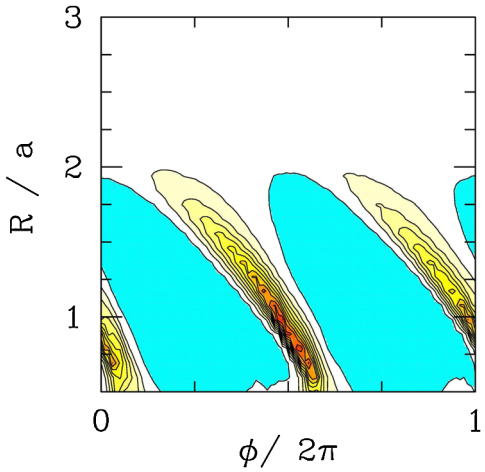

FIG. 7 (color online). Time-averaged surface density fluctuation $(\Sigma - \langle\Sigma\rangle)/\langle\Sigma\rangle$ in the rotating frame in which the binary is at rest. The binary point masses are located at $R/a = 0.5$ and $\phi = (0, \pi)$. Red regions are density maxima and blue regions are density minima. Data is from run A2 with $\Gamma = 4/3$.

binary separation is reduced, the location of the resonance retreats farther inside $R_{\rm in}$, enabling less matter to be stripped from the inner edge of the disk, and reducing $\dot{M}_0$. The reduction in accretion similarly suppresses the electromagnetic luminosity generated near the BHs. This effect is exacerbated by the reduction in shock heating due to binary torques, as this lowers the temperature of the gas and reduces emissivities. Each of these effects is reflected in Fig. 11. We also show the h_+ polarization amplitude of the accompanying gravitational wave for comparison. Evidently, the decrease in electromagnetic luminosity beginning at the onset of decoupling is a precursor to the late inpiral and merger gravitational radiation. We find that the choice of EOS can play a significant role in setting the magnitude of the accretion rate and the luminosity. Larger values of Γ lead to both larger $\dot{M}_0$ as well as higher

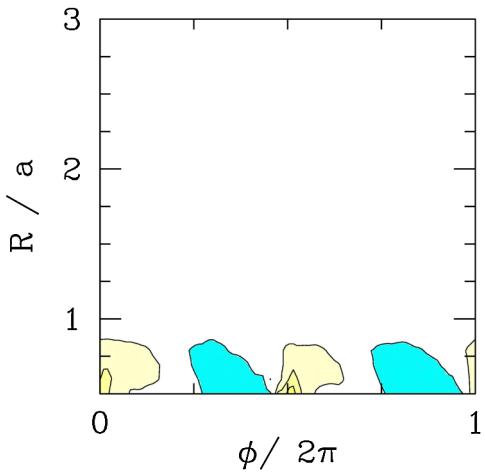

FIG. 8 (color online). Same as Fig. 7 but for a retrograde disk.

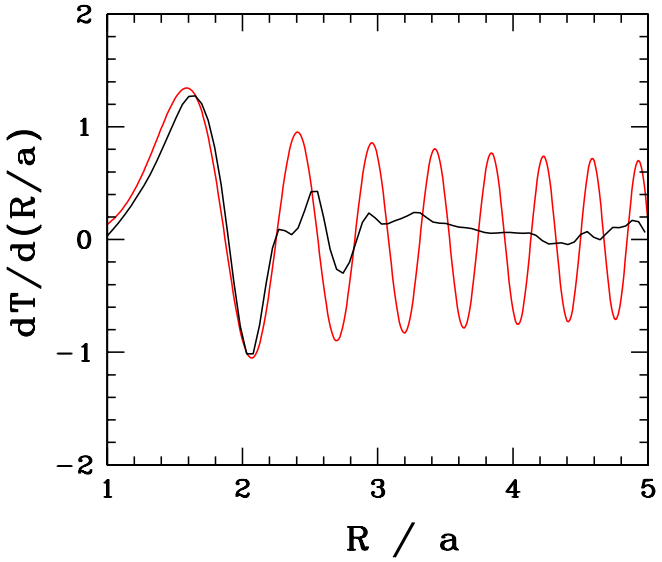

FIG. 9 (color online). Time-averaged torque density dT/dR exerted by the binary on the disk after $t \gtrsim 5t_{\rm disk}$. Time averaging was carried out over $\sim 2t_{\rm orb}$ after the disk has reached a quasistationary state. Data from run A2 with $\Gamma = 4/3$. The torque is plotted in units of $10^{-3}Ma\Sigma_0$.

luminosities. We tabulate the values of luminosities, accretion rates, and characteristic frequencies of emission at the onset of the late inspiral and merger epochs'' and just prior to merger in Table II. In addition to the increase in the amount of gas near the BHs, larger values of Γ also allow the gas to be shock heated more effectively. Because the bremsstrahlung and synchrotron emissivities are sensitive to temperature, this also leads to an increase in luminosity. Comparing Eqs. (54) and (55) below, we see that the temperature dependence is much stronger for synchrotron

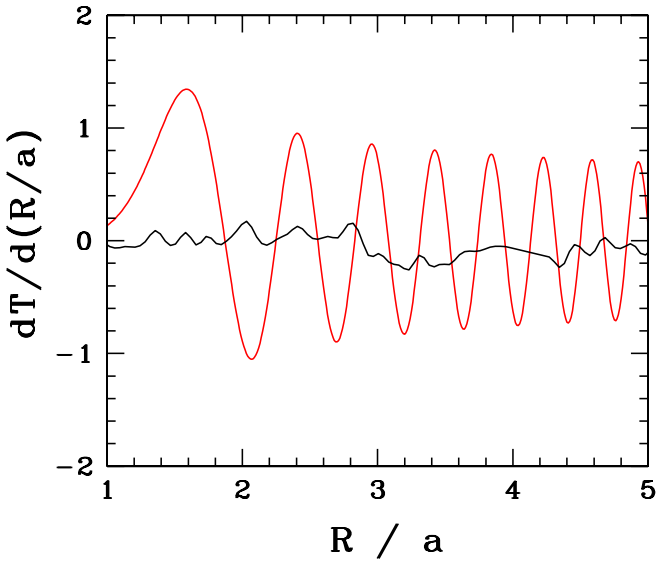

FIG. 10 (color online). Same as Fig. 9, but for retrograde disk (run A4).

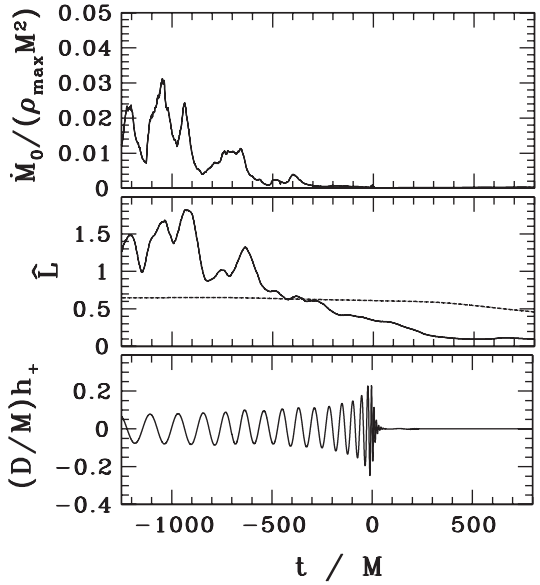

FIG. 11. Time evolution of total BH accretion rate across the BH horizons $\dot{M}_0$, luminosity $\hat{L}$ and waveform Dh_+ for a circumbinary prograde disk with $\Gamma = 5/3$. The initial binary separation is $a = 10M$ and the BHs evolve to merger. $\dot{M}_0/(\rho_{\rm max}M^2)$ is the dimensionless accretion rate. Here, $\rho_{\rm max}M^2 = 0.2n_{12}M_8^2M_\odot\ {\rm yr}^{-1}$. $\hat{L} \equiv L/[10^{46}M_8^3n_{12}^2\ {\rm erg\,s}^{-1}]$ is the total luminosity due to bremsstrahlung (dashed line) and synchrotron (solid line) emission. For synchrotron emission, we assume $\beta = 10$. h_+ is the + polarization of the gravitational wave signal as measured by an observer looking down the polar axis at a distance D from the binary. BHBH merger occurs at $t = 0$.

emission. This can explain the particularly large differences in synchrotron luminosity for the different cases reported in Table II. This effect also leads the synchrotron luminosity to be dominated by emission from the heated region near the binary, whereas the bremsstrahlung emission is predominantly from the bulk of the disk. This dependence accounts for the high variability of the synchrotron luminosity in comparison to that of the bremsstrahlung emission.

Because our simulations assume a perfect fluid with no dynamical magnetic fields (turbulent fields are assumed only to estimate synchrotron emission), there is no viscosity present to counteract the effect of the binary torques in driving matter outward. As a result, we find that even after relaxing to a quasistationary disk state in our early inspiral epoch calculations, in which the accretion rate and luminosity oscillate around fixed values, there remains an overall slow outward drift in the bulk of the disk. This is evident in Fig. 6, in which the solid red curve shows the surface density profile at the beginning of the binary inspiral, while the solid black curve shows the surface density profile at $t \sim t_{\rm disk}$ after the merger. We see clear evidence that the bulk of the disk moves outward, although we suspect that this effect may be altered by the inclusion of viscosity.

In Paper I, we demonstrated that shocks near the BH horizons increased in strength throughout the merger as the

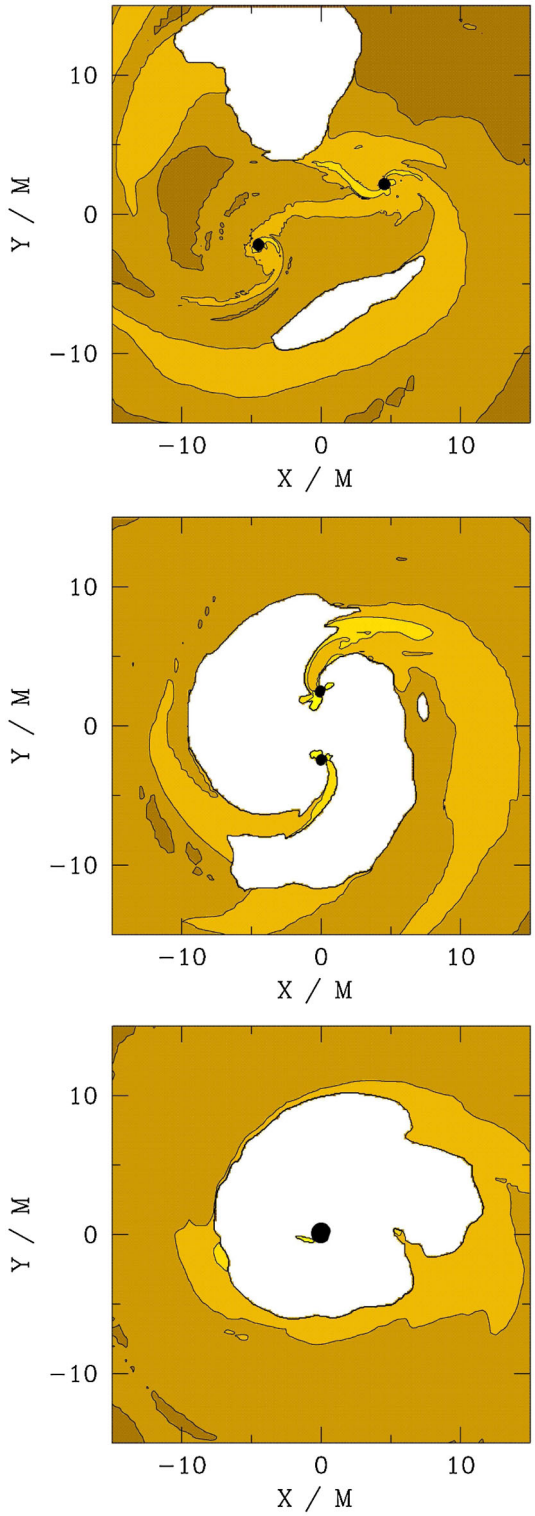

FIG. 12 (color online). Contours of temperature kT $(= m_B P/\rho_0)$ at select times for prograde disk with $\Gamma = 5/3$. Contours correspond to $\mathrm{kT} = 940 \times 10^{-5+0.66j}$ MeV $(j = 1, 2, \ldots, 6)$. Frames correspond to the beginning of the late inspiral and merger epochs phase at $t \approx t_{\mathrm{merge}} - 1250M$ (top), $t \sim t_{\mathrm{merge}} - 50M$ (middle), and $t \sim t_{\mathrm{merge}} + t_{\mathrm{disk}}$ (bottom). Regions with density less than $\rho_0/\rho_{0,\mathrm{max}} < 10^{-4.5}$ are left white. Lighter shading denotes higher kT.

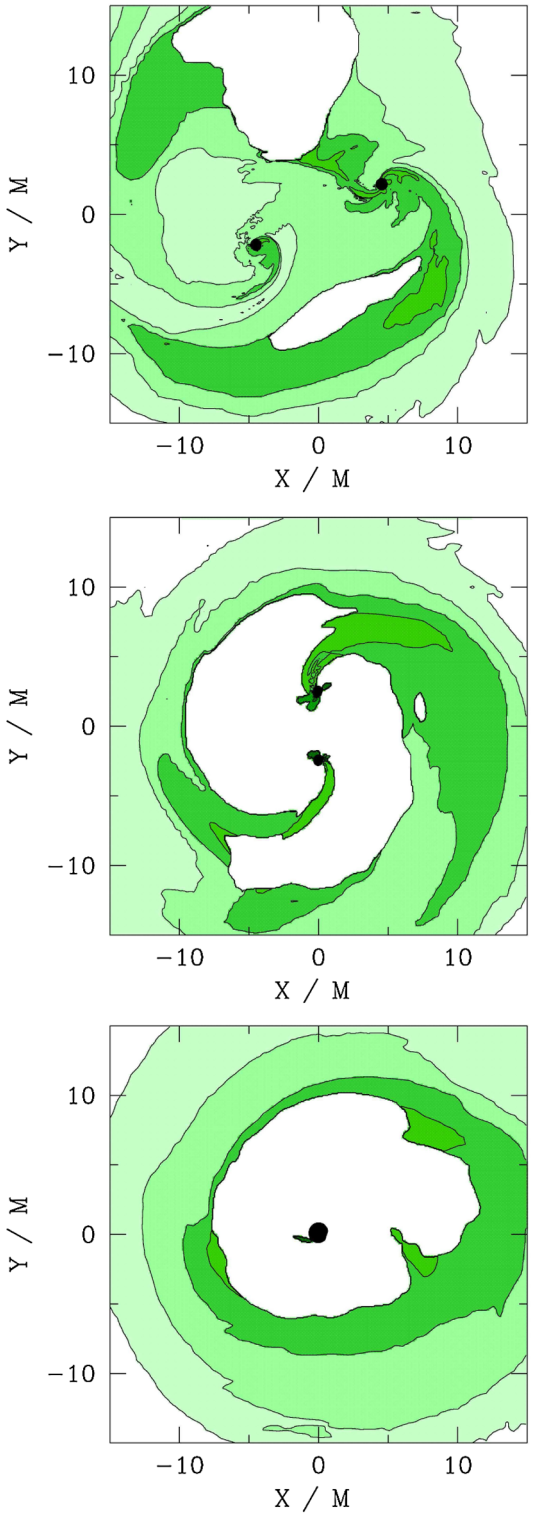

FIG. 13 (color online). Contours of entropy parameter K $(= P/\rho_0^{\Gamma})$ at select times for prograde disk with $\Gamma = 5/3$. Contours correspond to $K/K_0 = 10^{2+0.66j}$ $(j = 1, 2, \ldots, 6)$. Frames correspond to the beginning of the late inspiral and merger epochs phase at $t \approx t_{\mathrm{merge}} - 1250M$ (top), $t \sim t_{\mathrm{merge}} - 50M$ (middle), and $t \sim t_{\mathrm{merge}} + t_{\mathrm{disk}}$ (bottom). Regions with density less than $\rho_0/\rho_{0,\mathrm{max}} < 10^{-4.5}$ are left white. Darker shading denotes higher K.

BHs move more supersonically through the surrounding gas. This shock strengthening leads to a temperature increase in the inner region, which in turn gives rise to an increasing luminosity peaking at the moment of merger. Such a temperature increase is largely absent in the disklike accretion case treated here, as can be seen by comparing temperature contours at the beginning of the late inspiral and merger epochs simulation and at $t \sim t_{\rm merge} - 50M$, as displayed in Fig. 12. As such, we do not expect to see significant increase in luminosity during the post-decoupling inspiral phase, even at high-frequency components of the spectrum. We note that this contrasts the conclusions of the Newtonian calculation in [15], where a brightening of the precursor light curve before merger is found. However, these results do not necessarily contradict one another, as the authors of [15] consider geometrically thin, optically thick disks around non-equal-mass BHBH binaries. This is a very different scenario from the geometrically thick, optically thin disks surrounding equal-mass binaries that we consider in this paper.

To highlight the role that shock heating plays in our simulations, we also plot contours of K/K_0. Here $K \equiv P/\rho_0^\Gamma$ and K_0 is the initial value of K everywhere. The quantity $K = K(s)$, where s is the specific gas entropy, remains constant in the absence of shocks; shock heating yields $K/K_0 > 1$ (see Appendix B of [83]). As expected, we see that K/K_0 increases steeply near the BHs, where the binary torque-induced spiral arms are strongest (see Fig. 13). Following the merger, binary torques are no longer present and we find that K/K_0 is dramatically reduced in the cavity region. While we do find that a small region near the remnant continues to have K/K_0 long after the merger (see Fig. 13), we note that the gas in this region is of very low density and carries a relatively insignificant amount of thermal energy.

We also note that the shocks are confined to the inner region and do not propagate into the bulk of the disk. While it has been proposed that changes in the potential due to mass loss and/or BH kicks following merger can give rise to shocks throughout the disk [11,94], we do not observe such behavior in our simulations. However, this is expected, as it has been noted that a condition for shocks to form due to mass loss is that $\epsilon > H/R$, where $\epsilon \equiv (M_i - M_f)/M_i$ is the fractional mass loss due to gravitational wave emission [11]. Comparing the fractional mass loss for an equal-mass merger, for which $\epsilon \approx 0.05$, to the estimates of H/R measured at the moment of binary merger (see Table I), we find that the above condition is never satisfied. The criteria above for shocks to form is derived from the condition that the radial velocity must exceed the sound speed $c_s \equiv (\Gamma P/\rho_0 h)^{1/2}$ near the inner edge of the disk. We have also checked this directly and have found that the condition is never met in our simulations; our disks are too hot, hence too geometrically thick, to trigger this effect.

C. Scaling and detectability

In quoting values for the accretion rate $\dot{M}_0$, we normalize by the quantity $\rho_{\rm max} M^2 = 0.2 n_{12} M_8^2 M_\odot\ {\rm yr}^{-1}$, which allows for easy scaling to arbitrary disk density and binary mass. It is also possible to derive simple scaling relations for the luminosities. The dominant region of emission differs for bremsstrahlung and synchrotron radiation. Because of the stronger dependence of synchrotron emissivity on temperature (see Appendix B of [16]), we find that the synchrotron emission originates chiefly from the hot gas near the BHs, while the majority of bremsstrahlung emission originates from the cooler, denser gas in the bulk of the disk. In each simulation, we find that the temperature is maximum near the BHs, typically reaching $kT_h \approx 100$ MeV at the horizon. In the high-temperature limit ($kT > m_e c^2$) the synchrotron emissivity given in Appendix B of [16] scales with temperature and density according to

$$q_{\rm syn} \propto n_h^2 T_h^3 \beta^{-1}. \tag{54}$$

By contrast, the temperature in the bulk of the disk where the majority of the bremsstrahlung emission originates is nonrelativistic ($kT_{\rm disk} < m_e c^2$) so that the bremsstrahlung emissivity scales according to

$$q_{ff} \propto n_{\rm disk}^2 T_{\rm disk}^{1/2}. \tag{55}$$

Here n_h and T_h refer to the density and temperature at the horizon, and $n_{\rm disk}$ and $T_{\rm disk}$ refer to the density and temperature at $R_{\rm disk}$, and $\beta \equiv 8\pi P/B^2$ sets the strength of the assumed turbulent magnetic field responsible for synchrotron emission. As in Paper I, we choose $\beta = 10$ so that the magnetic field is assumed to reach a fraction of its equipartition value consistent with MHD simulations [81].

Integrating Eqs. (54) and (55), we find

$$L_{\rm syn} \approx \int dV q_{\rm syn} \propto n_h^2 T_h^3 \beta^{-1} M^3, \tag{56}$$

$$L_{ff} \approx \int dV q_{ff} \propto n_{\rm disk}^2 T_{\rm disk}^{1/2} R_{\rm disk}^3 (H/R), \tag{57}$$

where the factor of M^3 comes from the volume element.

Because we ignore self-gravity in the disk, our scaling results apply for arbitrary density. Accordingly, as the density at the horizon is varied, its value is simply proportional to the maximum density in the disk, $n_h \propto n_{\rm disk} \propto \rho_{\rm max}$.

Consider the onset of the binary decoupling (late inspiral) phase. The spiral arms through which the gas enters the disk cavity are shock heated. The gas in any shocked region will be heated to $kT \sim m_B v^2$. Since $v \lesssim c$ near the horizon, shock heating guarantees that $kT_h \lesssim m_B c^2 \sim 10^3$ MeV, independent of the temperature in the bulk of the disk (in fact KT_h is closer to 100 MeV). Scaling for synchrotron luminosity then simplifies to

$$L_{\rm syn} \propto \rho_{\rm max}^2 \beta^{-1} M^3. \tag{58}$$

While the bremsstrahlung luminosity does depend on $T_{\rm disk}$, we note that for the fixed values of q, $l(R_{\rm in})$, and $R_{\rm in}/M$ specified in Eqs. (A17)–(A19), the enthalpy profile h, and therefore $kT_{\rm disk} = m_B(h_{\rm disk} - 1)(\Gamma - 1)/\Gamma$, is uniquely specified. We therefore regard $T_{\rm disk}$ as a fixed parameter, so that

$$L_{ff} \propto \rho_{\rm max}^2 M^3. \tag{59}$$

Using these scaling relations, along with the results of our simulations, we estimate the average luminosity when the binary separation is $a = 10M$, the adopted onset of the late inspiral and merger epochs. Results are given in Table II.

In calculating the luminosity, we have assumed that the gas is optically thin. We can verify that this is a good assumption by estimating the optical depth. Taking the dominant opacity source to be electron scattering, we find

$$\tau_{es} \approx n_h \sigma_T R \sim 0.2 n_{12} M_8, \tag{60}$$

where R is the characteristic size of the emission region that we have set to $R \approx 2M$. Thus, we see that our assumption of an optically thin gas is valid for our canonical parameters, although it begins to break down when we consider denser disks and/or more massive binaries.

For bremsstrahlung emission originating at $R_{\rm disk}$, the characteristic observed frequency of the emission is given by

$$h\nu_{ff} \sim kT_{\rm disk}/(1 + z) \tag{61}$$

for a source at redshift z. We measure the temperature at $R_{\rm disk}$ for each of our cases, and report the estimated characteristic frequencies in Table II. For canonical parameters, bremsstrahlung emission will be predominantly in γ rays. Based on our measured luminosities, we estimate that the observed flux from this emission will be in the range of $\sim 10^{-15}$–$10^{-14} n_{12}^2 M_8^3$ erg cm^{-2} s^{-1} for a source at $z = 1$. Unfortunately, it is unlikely that this emission is strong enough to be detectable. We note that the bremsstrahlung emission we measure is actually dominated by emission from the bulk of the disk rather than the heated gas near the BHs. This makes the emission even less likely to be detectable, as it exhibits only a small amount of variability.

In contrast, the synchrotron emission is predominantly produced near the BHs. We can estimate the characteristic frequency of the synchrotron emission by noting that Eq. (B10) of [16] is maximized when $x_M \equiv 2\nu/3\nu_0\theta^2 \approx 1.09$. Here, $\nu_0 \equiv eB/2\pi m_e c$ is the cyclotron frequency and $\theta \equiv kT/m_e c^2$. The corresponding observed frequency is

$$h\nu_{\rm syn} = \frac{1.09}{1 + z} \frac{3ehB}{4\pi m_e c} \left(\frac{kT}{m_e c^2}\right)^2. \tag{62}$$

We can use this expression, along with measured values of density and temperature in the vicinity of the horizon, to estimate characteristic values of $h\nu_{\rm syn}$. Values for each case at the moment of decoupling and shortly before merger are given in Table II, and typically fall in the infrared range. We estimate that in each case, the synchrotron emission should be observable by the proposed Wide Field Infrared Survey Telescope (WFIRST) [95], and possibly by the Large Synoptic Survey Telescope instrument (LSST) [96]. Our simulations follow the late stage of the inspiral in which the binary separation decreases from $d = 10M$ to merger. This corresponds to a time scale of $\delta t \sim 100 M_8$ h during which the gradual decline in emission should be observed.

VI. DISCUSSION

In this paper we have performed a set of fully general-relativistic simulations of BHBH binary mergers in a circumbinary disk. Our focus has been identifying an observable electromagnetic signal that may accompany the gravitational waves from a black hole merger. Our simulations are exploratory only. We have restricted our attention to disklike accretion onto equal-mass, nonspinning BH binaries, although our methods may be extended to other binary configurations. We exploit the approximate helical Killing symmetry to determine the binary spacetime for widely separated BHBHs. The disk we evolve in this early inspiral spacetime relaxes to near quasiequilibrium. Our late inspiral and merger simulations begin with such a quasistationary disk. We then evolve the field as well as the matter. This epoch corresponds to the post disk-binary decoupling phase, terminating after merger, but before viscosity fills in the hollow.

For each simulation, we have calculated the time-varying rest-mass accretion rate, as well as the electromagnetic luminosity due to bremsstrahlung and synchrotron emission. We also derive scaling relations for the luminosity, enabling our results to be applied to a range of gas parameters and BH masses.

In each case, we find evidence for a time-varying electromagnetic signature accompanying the BHBH binary merger. The synchrotron emission is the most easily detectable component, and we observe a steady decline in synchrotron luminosity throughout the post-decoupling binary inspiral. This change serves as a characteristic precursor of a binary merger and should be detectable by the proposed WFIRST and possibly by the LSST instrument.

In Paper I, we restricted our attention to Bondi-like accetion onto merging binaries. It is instructive to compare the electromagnetic signatures associated with binary Bondi accretion with the signatures from disklike accretion discussed in this paper. In the binary Bondi case, there is a steady supply of gas accreting onto the binary at all stages of the merger. In this case, the evolution of the luminosity is determined by the strength of shock heating near the BHs. As the separation decreases, the BHs orbit more rapidly, and the shock-heated temperature of the gas increases. This increase leads to a luminosity that increases

throughout the inspiral, then drops precipitously following the merger as the shocks dissipate. This scenario is quite different from the case of disklike accretion, in which binary torques create a hollow region around the binary as well as a small amount of matter that leaks into the hollow in the form of spiral arms. Because the torques decrease throughout the inspiral as the BH separation decreases, we find that the accretion rate and luminosity decrease steadily over the course of our inspiral simulations.

We suspect, however, that this picture will change with the addition of magnetic fields, as the magneto-rotational instability will lead to turbulence. We intend to investigate this behavior in future calculations, although we expect that our results for the late inspiral and merger epochs treated here will not be significantly altered. The reason is that the time scale for turbulent viscosity to fill the hollow with gas for accretion exceeds the inspiral time scale following decoupling.

It is not possible to make a quantitative comparison of our results with those of Bode *et al* [49] due to significant differences in our methods. We employ disk solutions with power-law rotation dependence [72] and BHBH CTS metric data that we allow to relax over a time scale of $\sim 5t_{\rm disk} \approx 6000M$ before we begin our inspiral calculations. By contrast, Bode *et al* employ the constant midplane density initial data of [11] and relax this profile for a period of $\sim 250M$. Our calculations also differ significantly in that we consider bremmstrahlung radiation from the entire disk, whereas they consider only the cavity region near the BHs. We calculate the synchrotron emission as well. Nevertheless, we are able to see a qualitative agreement in the evolution of the rest-mass accretion rate $\dot{M}_0$, as a decline in $\dot{M}_0$ is observed throughout the inspiral phase in both calculations.

ACKNOWLEDGMENTS

We would like to thank Z. Etienne, C. Gammie, and V. Paschilidis for useful discussions. We are also grateful to H. Pfeiffer for providing CTS initial data for the BHBH spacetime metric. This paper was supported in part by NSF Grants No. PHY06-50377 and No. PHY09-63136 as well as NASA Grants No. NNX07AG96G and No. NN11AE11G. B. Farris gratefully acknowledges support from NASA, NNX09AO64H.

APPENDIX A: DISK INITIAL DATA

Our formulation for an equilibrium stationary disk around a *single* Kerr BH follows closely that of [72,73].

From the conservation of the stress-energy equation, we find

$$0 = T^{\beta}{}_{\alpha;\beta} = \frac{1}{\alpha\sqrt{\gamma}}(\alpha\sqrt{\gamma}T_{\alpha}{}^{\beta})_{,\beta} - \Gamma^{\lambda}_{\alpha\mu}T^{\mu}_{\lambda} \tag{A1}$$

$$= \frac{1}{\alpha\sqrt{\gamma}}(\alpha\sqrt{\gamma}\rho_0 h u_{\alpha}u^{\beta})_{,\beta} \tag{A2}$$

$$+ P_{,\alpha} + \frac{1}{2}(g^{\mu\nu}{}_{,\alpha}\rho_0 h u_{\mu}u_{\nu}). \tag{A3}$$

Since we are seeking a solution for a stationary torus in Kerr spacetime for a single BH, we can now impose time independence, axisymmetry, and no poloidal or radial motion:

$$\partial_t(\ldots) = \partial_{\phi}(\ldots) = 0, \tag{A4}$$

$$u^r = u^{\theta} = 0. \tag{A5}$$

In Boyer-Lindquist and Kerr-Schild coordinates, these constraints imply that $u_r = u_{\theta} = 0$.

We may now simplify Eq. (A3) according to

$$0 = \frac{h_{,j}}{h} - \frac{1}{2}u_t^2(u_t^{-2})_{,j} - \frac{\Omega}{1 - l\Omega}l_{,j}. \tag{A6}$$

Here we have also assumed constant entropy, and we have introduced the specific angular momentum $l \equiv -u_{\phi}/u_t$. We have also used the fact that $u^{\mu}u_{\mu} = -1$ to show that

$$u_t^{-2} = -(g^{tt} - 2lg^{t\phi} + l^2 g^{\phi\phi}), \tag{A7}$$

and have defined

$$\Omega \equiv u^{\phi}/u^t = (g^{t\phi} - lg^{\phi\phi})/(g^{tt} - lg^{t\phi}). \tag{A8}$$

We now follow [72,73] and assume the disk has a power-law rotation dependence, whereby Ω takes the form

$$\Omega = \eta\lambda^{-q}, \tag{A9}$$

where

$$\lambda^2 \equiv \frac{l}{\Omega} = l\frac{g^{tt} - lg^{t\phi}}{g^{t\phi} - lg^{\phi\phi}}. \tag{A10}$$

Combining Eq. (A9) and (A10), we find that

$$\Omega = kl^{\alpha}, \tag{A11}$$

where $\alpha \equiv q/(q-2)$ and $k = \eta^{-2/(q-2)}$.

It is now straightforward to show that Eq. (A6) is satisfied by

$$h(r,\theta) = \frac{u_{t,\rm in}f(l_{\rm in})}{u_t(r,\theta)f(l(r,\theta))}, \tag{A12}$$

where $f(l) = |1 - kl^{\alpha+1}|^{1/(\alpha+1)}$. A disk solution is uniquely determined for fixed $R_{\rm in}$, $l(R_{\rm in})$, and q.

While the solution described above applies to equilibrium disks in general Kerr spacetimes, we assume a Schwarzschild geometry for the purposes of this study.

In the Newtonian limit, we know that $l = \Omega r^2$, so $\lambda^2 = l/\Omega = r^2$, whereby

$$\Omega \propto \lambda^{-q} \propto r^{-q}. \tag{A13}$$

Thus we can see that asymptotically,

$$q = 0 \Rightarrow \Omega = \text{const}, \tag{A14}$$

$$q = 2 \Rightarrow l = \text{const}, \tag{A15}$$

$$q = 1.5 \Rightarrow \text{Keplerian}. \tag{A16}$$

In this paper, the following parameters are chosen to determine the initial disk configuration (set close to Keplerian),

$$q = 1.6, \tag{A17}$$

$$l(R_{\text{in}}) = 4.53, \tag{A18}$$

$$R_{\text{in}} = 15M. \tag{A19}$$

APPENDIX B: DERIVATION OF THE TORQUE DENSITY dT/dR

If we consider a four vector $\vec{j}$ that is not necessarily conserved, then we must generalize Eq. (27) to

$$\frac{dq}{dt} = -\mathcal{F}_H + \mathcal{F}_L + \int \sqrt{-g}\nabla_\mu j^\mu d^3x. \tag{B1}$$

If we choose to set H and L to be two concentric cylinders of infinite extent, centered around the z axis and of radius R and $R + \delta R$, respectively, we can rewrite Eq. (B1) as

$$\frac{d}{dt}(q(R+\delta R) - q(R)) = -\mathcal{F}(R) + \mathcal{F}(R+\delta R) + \int \sqrt{-g}\nabla_\mu j^\mu R dR dz d\phi \tag{B2}$$

taking the limit $\delta R \to 0$, we therefore find that

$$\frac{d}{dR}\left(\frac{dq}{dt}\right) = \frac{d\mathcal{F}}{dR} + \int \sqrt{-g}\nabla_\mu j^\mu R dz d\phi. \tag{B3}$$

We can consider the specific case where $j^\mu = T^\mu{}_\nu \phi^\nu$, and $\phi^\nu \equiv (\partial_\phi)^\mu = (0, -y, x, 0)$, so that Eq. (B3) becomes

$$\frac{d}{dR}\left(\frac{dJ}{dt}\right) \equiv \frac{dT_{\text{tot}}}{dR} = \frac{d\mathcal{F}^{(J)}}{dR} + \int \sqrt{-g}T^{\mu\nu}\nabla_\mu \phi_\nu R dz d\phi. \tag{B4}$$

We interpret the first term on the right-hand side of Eq. (B4) as arising from the net outflow of angular momentum carried by matter across the surfaces at R and $R + \delta R$, while the second term is the torque due to the gravitational field. Because we are most interested in the torque from the gravitational field of the binary, we define

$$\frac{dT}{dR} \equiv \frac{dT_{\text{tot}}}{dR} - \frac{d\mathcal{F}^{(J)}}{dR} = \int \sqrt{-g}T^{\mu\nu}\nabla_\mu \phi_\nu R dz d\phi. \tag{B5}$$

Note that in an axisymmetric spacetime in which ϕ_ν is a Killing vector field, $T^{\mu\nu}\nabla_\mu \phi_\nu = T^{\mu\nu}\nabla_{(\mu}\phi_{\nu)} = 0$, hence $dT/dR = 0$ as expected.

In order to compute Eq. (B5) numerically, it is convenient to transform the expression into Cartesian coordinates. Note that

$$\begin{aligned} T^{\mu\nu}\nabla_\mu \phi_\nu &= T^\mu{}_\nu \nabla_\mu \phi^\nu \\ &= T^\mu{}_\nu(\phi^\nu_{,\mu} + \Gamma^\nu{}_{\sigma\mu}\phi^\sigma) \\ &= T^\mu{}_\nu \phi^\nu_{,\mu} + \tfrac{1}{2}T^{\mu\nu}g_{\mu\nu,\sigma}\phi^\sigma \\ &= -T^\mu{}_x y_{,\mu} + T^\mu{}_y x_{,\mu} + \tfrac{1}{2}T^{\mu\nu}(-g_{\mu\nu,x}y + g_{\mu\nu,y}x) \\ &= -T^y{}_x + T^x{}_y - \tfrac{1}{2}yT^{\mu\nu}g_{\mu\nu,x} + \tfrac{1}{2}xT^{\mu\nu}g_{\mu\nu,y}. \end{aligned} \tag{B6}$$

Inserting Eq. (B6) into Eq. (B5), we find

$$\frac{dT}{dR} = \int R d\phi dz \sqrt{-g}(-T^y{}_x + T^x{}_y) + \frac{1}{2}\int R d\phi dz \sqrt{-g}(-yT^{\mu\nu}g_{\mu\nu,x} + xT^{\mu\nu}g_{\mu\nu,y}). \tag{B7}$$

Equation (B7) is integrated numerically at a number of different radii, so that we can compute profiles of dT/dR.

Newtonian limit

We can check that Eq. (B7) reduces to the correct expression in the Newtonian limit. If we let $T^{00} \approx \rho_0$, $|T^{0i}/T^{00}| \ll 1$, and $|T^{ij}/T^{00}| \ll 1$, we find

$$\begin{aligned} \frac{dT}{dR} &\approx \frac{1}{2}\int R d\phi dz T^{00}(-yg_{00,x} + xg_{00,y}) \\ &= \frac{1}{2}\int R d\phi dz T^{00} g_{00,\phi} \\ &= -\int R d\phi dz \rho_0 \Phi_{,\phi} \\ &= -2\pi R\langle \Sigma \Phi_{,\phi}\rangle, \end{aligned} \tag{B8}$$

where angled brackets indicate angle averaging, and Φ is the Newtonian gravitational potential. Equation (B8) matches the expression given in Eq. (14) of [36].

[1] D. Richstone, E. A. Ajhar, R. Bender, G. Bower, A. Dressler, S. M. Faber, A. V. Filippenko, K. Gebhardt, R. Green, L. C. Ho, J. Kormendy, T. R. Lauer, J. Magorrian, and S. Tremaine, Nature (London) **395**, A14 (1998).

[2] B. M. Peterson and A. Wandel, Astrophys. J. Lett. **540**, L13 (2000).

[3] L. Ferrarese and H. Ford, Space Sci. Rev. **116**, 523 (2005).

[4] M. C. Begelman, R. D. Blandford, andM. J. Rees, Nature (London) **287**, 307 (1980).

[5] N. Roos, Astron. Astrophys. **104**, 218 (1981).

[6] D. Merritt and M. Milosavljević, Living Rev. Relativity **8**, 8 (2005).

[7] M. Milosavljević and E. S. Phinney, Astrophys. J. Lett. **622**, L93 (2005).

[8] E. M. Rossi, G. Lodato, P. J. Armitage, J. E. Pringle, and A. R. King, Mon. Not. R. Astron. Soc. **400**, 1726 (2009).

[9] J. D. Schnittman and J. H. Krolik, Astrophys. J. **684**, 835 (2008).

[10] L. R. Corrales, Z. Haiman, and A. MacFadyen, Mon. Not. R. Astron. Soc. **404**, 947 (2010).

[11] S. M. O'Neill, M. C. Miller, T. Bogdanović, C. S. Reynolds, and J. D. Schnittman, Astrophys. J. **700**, 859 (2009).

[12] S. L. Shapiro, Phys. Rev. D **81**, 024019 (2010).

[13] T. Tanaka and K. Menou, Astrophys. J. **714**, 404 (2010).

[14] P. J. Armitage and P. Natarajan, Astrophys. J. Lett. **567**, L9 (2002).

[15] P. Chang, L. E. Strubbe, K. Menou, and E. Quataert, Mon. Not. R. Astron. Soc. **407**, 2007 (2010).

[16] B. D. Farris, Y. T. Liu, and S. L. Shapiro, Phys. Rev. D **81**, 084008 (2010).

[17] H. L. Maness, G. B. Taylor, R. T. Zavala, A. B. Peck, and L. K. Pollack, Astrophys. J. **602**, 123 (2004).

[18] C. Rodriguez, G. B. Taylor, R. T. Zavala, A. B. Peck, L. K. Pollack, and R. W. Romani, Astrophys. J. **646**, 49 (2006).

[19] C. Rodriguez, G. B. Taylor, R. T. Zavala, Y. M. Pihlström, and A. B. Peck, Astrophys. J. **697**, 37 (2009).

[20] H. J. Lehto and M. J. Valtonen, Astrophys. J. **460**, 207 (1996).

[21] M. J. Valtonen, H. J. Lehto, A. Sillanpää, K. Nilsson, S. Mikkola, R. Hudec, M. Basta, H. Teräsranta, S. Haque, and H. Rampadarath, Astrophys. J. **646**, 36 (2006).

[22] M. J. Valtonen *et al.*, Nature (London) **452**, 851 (2008).

[23] T. Bogdanovíc, M. Eracleous, and S. Sigurdsson, Astrophys. J. **697**, 288 (2009).

[24] M. Dotti, C. Montuori, R. Decarli, M. Volonteri, M. Colpi, and F. Haardt, Mon. Not. R. Astron. Soc. **398**, L73 (2009).

[25] S. Komossa, H. Zhou, and H. Lu, Astrophys. J. Lett. **678**, L81 (2008).

[26] T. A. Boroson and T. R. Lauer, Nature (London) **458**, 53 (2009).

[27] X. Liu, Y. Shen, and M. A. Strauss, arXiv:1104.3391.

[28] B. Kocsis, Z. Haiman, and K. Menou, Astrophys. J. **684**, 870 (2008).

[29] C. Deffayet and K. Menou, Astrophys. J. Lett. **668**, L143 (2007).

[30] D. E. Holz and S. A. Hughes, Astrophys. J. **629**, 15 (2005).

[31] B. Kocsis, Z. Frei, Z. Haiman, and K. Menou, Astrophys. J. **637**, 27 (2006).

[32] T. Tanaka, Z. Haiman, and K. Menou, Astron. J. **140**, 642 (2010).

[33] P. Artymowicz and S. H. Lubow, Astrophys. J. **421**, 651 (1994).

[34] R. Günther and W. Kley, Astron. Astrophys. **387**, 550 (2002).

[35] A. Escala, R. B. Larson, P. S. Coppi, and D. Mardones, Astrophys. J. **630**, 152 (2005).

[36] A. I. MacFadyen and M. Milosavljević, Astrophys. J. **672**, 83 (2008).

[37] M. Megevand, M. Anderson, J. Frank, E. W. Hirschmann, L. Lehner, S. L. Liebling, P. M. Motl, and D. Neilsen, Phys. Rev. D **80**, 024012 (2009).

[38] M. Campanelli, C. O. Lousto, Y. Zlochower, and D. Merritt, Phys. Rev. Lett. **98**, 231102 (2007).

[39] T. Bogdanović, C. S. Reynolds, and M. C. Miller, Astrophys. J. Lett. **661**, L147 (2007).

[40] M. Anderson, L. Lehner, M. Megevand, and D. Neilsen, Phys. Rev. D **81**, 044004 (2010).

[41] G. A. Shields and E. W. Bonning, Astrophys. J. **682**, 758 (2008).

[42] Z. Lippai, Z. Frei, and Z. Haiman, Astrophys. J. Lett. **676**, L5 (2008).

[43] O. Zanotti, L. Rezzolla, L. Del Zanna, and C. Palenzuela, Astron. Astrophys. **523**, A8 (2010).

[44] J. R. van Meter, J. H. Wise, M. C. Miller, C. S. Reynolds, J. M. Centrella, J. G. Baker, W. D. Boggs, B. J. Kelly, and S. T. McWilliams, Astrophys. J. Lett. **711**, L89 (2010).

[45] P. Mösta, C. Palenzuela, L. Rezzolla, L. Lehner, S. Yoshida, and D. Pollney, Phys. Rev. D **81**, 064017 (2010).

[46] C. Palenzuela, L. Lehner, and S. L. Liebling, Science **329**, 927 (2010).

[47] T. Bode, R. Haas, T. Bogdanović, P. Laguna, and D. Shoemaker, Astrophys. J. **715**, 1117 (2010).

[48] T. Bogdanovic, T. Bode, R. Haas, P. Laguna, and D. Shoemaker, Classical Quantum Gravity **28**, 094020 (2011).

[49] T. Bode, T. Bogdanovic, R. Haas, J. Healy, P. Laguna, and D. Shoemaker, arXiv:1101.4684.

[50] M. Shibata and T. Nakamura, Phys. Rev. D **52**, 5428 (1995).

[51] T. W. Baumgarte and S. L. Shapiro, Phys. Rev. D **59**, 024007 (1998).

[52] H. Friedrich, Commun. Math. Phys. **100**, 525 (1985).

[53] D. Garfinkle, Phys. Rev. D **65**, 044029 (2002).

[54] F. Pretorius, Classical Quantum Gravity **22**, 425 (2005).

[55] F. Pretorius, Phys. Rev. Lett. **95**, 121101 (2005).

[56] M. Campanelli, C. O. Lousto, P. Marronetti, and Y. Zlochower, Phys. Rev. Lett. **96**, 111101 (2006).

[57] J. G. Baker, J. Centrella, D.-I. Choi, M. Koppitz, and J. van Meter, Phys. Rev. Lett. **96**, 111102 (2006).

[58] L. Blanchet, G. Faye, B. R. Iyer, and S. Sinha, Classical Quantum Gravity **25**, 165003 (2008).

[59] B. Aylott *et al.*, Classical Quantum Gravity **26**, 165008 (2009).

[60] J. D. Larwood and J. C. B. Papaloizou, Mon. Not. R. Astron. Soc. **285**, 288 (1997).

[61] P. B. Ivanov, J. C. B. Papaloizou, and A. G. Polnarev, Mon. Not. R. Astron. Soc. **307**, 79 (1999).

[62] Y. T. Liu and S. L. Shapiro, Phys. Rev. D **82**, 123011 (2010).
[63] H. P. Pfeiffer and J. W. York, Phys. Rev. D **67**, 044022 (2003).
[64] G. B. Cook and H. P. Pfeiffer, Phys. Rev. D **70**, 104016 (2004).
[65] T. W. Baumgarte and S. L. Shapiro, *Numerical Relativity: Solving Einstein's Equations on the Computer* (Cambridge University Press, Cambridge, England, 2010).
[66] F. K. Liu, X. Wu, and S. L. Cao, Mon. Not. R. Astron. Soc. **340**, 411 (2003).
[67] N. J. Turner, Astrophys. J. Lett. **605**, L45 (2004).
[68] D. Lynden-Bell and J. E. Pringle, Mon. Not. R. Astron. Soc. **168**, 603 (1974).
[69] Z. B. Etienne, J. A. Faber, Y. T. Liu, S. L. Shapiro, and T. W. Baumgarte, Phys. Rev. D **76**, 101503 (2007).
[70] M. D. Duez, Y. T. Liu, S. L. Shapiro, and B. C. Stephens, Phys. Rev. D **72**, 024028 (2005).
[71] J. R. van Meter, J. G. Baker, M. Koppitz, and D.-I. Choi, Phys. Rev. D **73**, 124011 (2006).
[72] S. K. Chakrabarti, Astrophys. J. **288**, 1 (1985).
[73] J. De Villiers, J. F. Hawley, and J. H. Krolik, Astrophys. J. **599**, 1238 (2003).
[74] Cactus code official Web site http://www.cactuscode.org/.
[75] E. Schnetter, S. H. Hawley, and I. Hawke, Classical Quantum Gravity **21**, 1465 (2004).
[76] J. Thornburg, Classical Quantum Gravity **21**, 743 (2004).
[77] P. Colella and P. R. Woodward, J. Comput. Phys. **54**, 174 (1984).
[78] A. Harten, P. D. Lax, and B van Leer, SIAM Rev. **25**, 35 (1983).
[79] Z. B. Etienne, J. A. Faber, Y. T. Liu, S. L. Shapiro, K. Taniguchi, and T. W. Baumgarte, Phys. Rev. D **77**, 084002 (2008).
[80] M. Shibata, M. D. Duez, Y. T. Liu, S. L. Shapiro, and B. C. Stephens, Phys. Rev. Lett. **96**, 031102 (2006).
[81] J. C. McKinney and C. F. Gammie, Astrophys. J. **611**, 977 (2004).
[82] Y. T. Liu, S. L. Shapiro, and B. C. Stephens, Phys. Rev. D **76**, 084017 (2007).
[83] Z. B. Etienne, Y. T. Liu, S. L. Shapiro, and T. W. Baumgarte, Phys. Rev. D **79**, 044024 (2009).
[84] J. A. Faber, T. W. Baumgarte, Z. B. Etienne, S. L. Shapiro, and K. Taniguchi, Phys. Rev. D **76**, 104021 (2007).
[85] B. D. Farris, T. K. Li, Y. T. Liu, and S. L. Shapiro, Phys. Rev. D **78**, 024023 (2008).
[86] M. Campanelli, C. O. Lousto, and Y. Zlochower, Phys. Rev. D **73**, 061501 (2006).
[87] K. Hayasaki, S. Mineshige, and H. Sudou, Publ. Astron. Soc. Jpn. **59**, 427 (2007).
[88] C. Roedig, M. Dotti, A. Sesana, J. Cuadra, and M. Colpi, arXiv:1104.3868.
[89] D. N. C. Lin, J. C. B. Papaloizou, and G. J. Savonije, Astrophys. J. **364**, 326 (1990).
[90] D. N. C. Lin, J. C. B. Papaloizou, and G. J. Savonije, Astrophys. J. **365**, 748 (1990).
[91] N. I. Shakura and R. A. Sunyaev, Astron. Astrophys. **24**, 337 (1973).
[92] I. D. Novikov and K. S. Thorne, in *Black Holes (Les Astres Occlus)* (Gordon and Breach, New York, 1973), pp. 343–450.
[93] S. L. Shapiro and S. A. Teukolsky, *Black Holes, White Dwarfs, and Neutron Stars: The Physics of Compact Objects* (Wiley, New York, 1983).
[94] N. Bode and S. Phinney, APS Meeting Abstracts, **10**, 10 (2007).
[95] WFIRST official Web site http://wfirst.gsfc.nasa.gov/.
[96] LSST official Web site http://www.lsst.org.